



HAL
open science

Scaling Analysis of the China France Oceanography Satellite Along-Track Wind and Wave Data

Yang Gao, François G Schmitt, Jianyu Hu, Yongxiang Huang

► **To cite this version:**

Yang Gao, François G Schmitt, Jianyu Hu, Yongxiang Huang. Scaling Analysis of the China France Oceanography Satellite Along-Track Wind and Wave Data. *Journal of Geophysical Research. Oceans*, 2021, 126 (8), pp.e2020JC017119. 10.1029/2020JC017119 . hal-03319667

HAL Id: hal-03319667

<https://hal.science/hal-03319667>

Submitted on 12 Aug 2021

HAL is a multi-disciplinary open access archive for the deposit and dissemination of scientific research documents, whether they are published or not. The documents may come from teaching and research institutions in France or abroad, or from public or private research centers.

L'archive ouverte pluridisciplinaire **HAL**, est destinée au dépôt et à la diffusion de documents scientifiques de niveau recherche, publiés ou non, émanant des établissements d'enseignement et de recherche français ou étrangers, des laboratoires publics ou privés.

Scaling Analysis of the China France Oceanography SATellite Along-Track Wind and Wave Data

Yang Gao^{1,2}, Francois G Schmitt², Jianyu Hu^{1,3}, Yongxiang Huang^{1,3,4,5}

¹State Key Laboratory of Marine Environmental Science, College of Ocean and Earth Sciences, Xiamen University, Xiamen 361102, China

²CNRS, Univ. Lille, Univ. Littoral Cote d'Opale, UMR 8187, LOG, Laboratoire d'Océanologie et de Géosciences, F 62930 Wimereux, France

³Southern Marine Science and Engineering Guangdong Laboratory (Zhuhai), Zhuhai 519000, China

⁴Fujian Engineering Research Center for Ocean Remote Sensing Big Data, Xiamen 361102, China

⁵SJTU SMSE-Mingguang Joint Research Center for Advanced Palygoskite Materials, Mingguang 239400, China

Key Points:

- Fourier power spectra are retrieved for both wind and wave fields simultaneously measured by the China France Oceanography SATellite.
- Due to a large scale separation, the multiscale scaling features for both wind and wave fields are observed from 100 to 3000 km.
- Meridional and seasonal variations of the scaling features are evident.

Corresponding author: Y.H., yongxianghuang@xmu.edu.cn

Abstract

Turbulence or turbulence-like phenomena are ubiquitous in nature, often showing a power-law behavior of the fluctuations in either spatial or temporal domains. This power-law behavior is due to interactions among different scales of motion, and to the absence of characteristic scale. In this work, we consider the multiscale dynamics of China France Oceanography SATellite (CFOSAT) data as atmospheric and oceanic quantities influenced by turbulence. Fourier power spectra were estimated for the data provided by the CFOSAT via the Wiener-Khinchine theorem to extract multiscale information for both wind speed (WS) and significant wave-height (Hs). The WS data were collected from December 18, 2018 to August 31, 2020, and the Hs data from July 29, 2019 to August 31, 2020. Fourier power spectra for both WS and Hs exhibit power-law features in the ranges of 100 km to 3000 km with a scaling exponent β varying from $5/3$ to 3. The global distributions and seasonal variations of β for both WS and Hs have also been considered. The results show that due to the energetic convective activities in the low-latitude zones, the scaling exponents β in these regions are closer to the value of $5/3$. Concerning the seasonal variations, for most regions, the scaling exponents in winter are larger than those in summer for WS. The seasonal variations of β in low-latitudes are stronger than those in the mid-latitudes. Our preliminary results enrich the fundamental knowledge of ocean surface processes and also provide a benchmark for either oceanic or atmospheric models.

Plain Language Summary

The China France Oceanography SATellite (CFOSAT) can measure simultaneously wind and wave, providing a unique data set to assess the coupling of the wind and wave during the air-sea interactions. Here we show that the multiscale spatial statistics is relevant for both wind and wave fields. More precisely, spatial scaling behavior is found on the spatial scale range of 100 km to 3000 km, with a scaling exponent varying on different oceans and seasons. Furthermore, the dynamical coupling between the wind and wave is characterized by the Fourier-based co-spectrum and coherence function analysis. The results obtained in our study not only enrich our fundamental knowledge of ocean surface processes, but also provide a benchmark for either oceanic or atmospheric models.

1 Introduction

Ocean waves and wind play critical roles at various scales as they regulate the functioning of Earth's climate and weather system (Bigg et al., 2003). The momentum and heat exchanges between the ocean and the atmosphere are affected by waves and wind. For example, some aerosols are generated by wave breaking and transported by wind (Kunz et al., 2002); the growth and decay of sea ice are influenced by waves and wind (Schlosser et al., 2018); waves and wind also show critical interactions with surface currents and upper ocean turbulence (Babanin, 2006), to list a few. Furthermore, waves and wind are major information for the safety of offshore operations and the forecast of marine severe weather events. Therefore, waves and wind, especially significant wave height (Hs) and wind speed (WS) are of interest for many fields from scientific researches to engineering applications.

The aims of studying the waves and wind are also to improve the ocean dynamic modeling and prediction, marine meteorology forecast, climate variability knowledge, and fundamental knowledge of surface processes (Hauser et al., 2016). Due to extremely high Reynolds numbers, the non-linearities and multiple spatial-temporal scales characterizing the ocean and atmosphere, it is hard to describe, simulate or predict their complicated motions precisely (Vallis, 2017). Most oceanic, atmospheric or global models are operated by averaging Navier-Stokes equations at large scales. Turbulent closures are needed to express the effects of small-scale fluxes to large scale processes, but exact expressions are still lacking (Pope, 2001; Schmitt, 2007; Egolf & Hutter, 2020), indicating that oceanic and atmospheric models have still fundamental weaknesses.

68 The foundation of studying the wind and waves comes from field observations. Relatively
 69 accurate measurements of wind speed were possible after the invention of the anemome-
 70 ter by Thomas Romney in 1846. Then, more precise wind speed observations have been
 71 achieved by the development of hot wire anemometers, while the wind could only be mea-
 72 sured in a fixed point, until the occurrence of Doppler radars. For estimating the wind at a
 73 global scale, a satellite onboard wind scatterometer was developed during the Seasat mission
 74 in the 1970s. After that, a series of satellites which can observe the wind field have been
 75 launched, such as Nimbus-7 (1979), Advanced Earth Observing Satellite (ADEOS, 1996),
 76 Quick Scatterometer (QuikSCAT, 1999), Meteorological Operational Satellites (METOP-A,
 77 METOP-B, and METOP-C, mission since 2006), Cyclone Global Navigation Satellite Sys-
 78 tem (CYGNSS, 2017), HaiYang-2B (HY-2B, 2018), to name a few. Before 1975, wave height
 79 data have been mainly collected by buoys or coastal marine observation stations. Since
 80 that year, global ocean wave heights could be retrieved by satellites equipped with radar
 81 altimeters, such as for instance, Geodetic Earth Orbiting Satellite-3 (GEOS-3, 1975), Euro-
 82 pean Remote-Sensing Satellite (ERS-1, 1991), Topography Experiment/Poseidon (TOPEX,
 83 1996), JASON-1 (2001), and followed by JASON-2 (2008), and JASON-3 (2016), HaiYang-
 84 2A (HY-2A, 2011), to list a few.

85 Previously, due to the limitation in the available data, the dynamic analysis of wind
 86 and waves have mostly been done separately. Since the ocean surface waves are most
 87 commonly driven by wind through frictions between wind and surface waters, the energy
 88 and momentum of waves are injected by the wind blowing over the sea surface. In some light
 89 WS regions, such as in the tropics, the energy and momentum can also be transferred back
 90 from waves to wind (Hanley et al., 2010). To determine the dynamical coupling between
 91 wind and waves, a detailed study of the multiscale properties of wind and waves is required.
 92 Thanks to the China France Oceanography SATellite (CFOSAT), the WS and Hs data can
 93 be observed simultaneously from space for the first time. The CFOSAT project provides a
 94 unique chance to analyze the wind and waves together at a global scale.

95 In this study, on the basis of the WS and Hs data observed by CFOSAT, Fourier power
 96 spectra are estimated via the Wiener-Khinchine theorem to study scaling properties and
 97 evaluate scaling ranges and slopes. In addition, the spatial and temporal variations of the
 98 scaling exponents are examined. In the following, firstly some theories for atmospheric wind
 99 scaling regimes are recalled, as well as for the oceanic waves. Then the data and methods
 100 are presented, followed by a section presenting the results, and two last sections are devoted
 101 to discussions and conclusions.

102 2 Theories

103 2.1 Theories for the Atmospheric Wind

104 Assuming that there are no characteristic length scales, over given scale ranges, several
 105 scaling laws have been proposed for the wind field in the atmosphere. Here these theoretical
 106 proposals are recalled briefly. They will be used as comparisons and potential explanations
 107 when considering the CFOSAT data analysis in the following sections.

108 The most classical scaling is Kolmogorov's 1941 assumption of universal fluctuations of
 109 the turbulent wind velocity in the inertial range, using locally isotropic and homogeneous
 110 hypotheses. For very large Reynolds numbers, as is the case in the atmosphere, one obtains
 111 (Kolmogorov, 1941; Obukhov, 1941):

$$E_u(k) = C_0 \epsilon^{-2/3} k^{-5/3}, \quad (1)$$

112 where $E_u(k)$ is the Fourier power spectrum of the wind velocity, ϵ is the mean energy
 113 dissipation rate per unit mass, k is one component of the wavenumber vector $\mathbf{k} = (k_x, k_y, k_z)$,
 114 and C_0 is a constant. In case of intermittency there may be some small corrections to
 115 the value of the spectral slope $-5/3$, with slopes that may be slightly steeper, e.g., an

116 experimental value of -1.70 has been reported (Monin & Yaglom, 1971; Frisch, 1995).
 117 This framework corresponds to a cascade of energy as proposed by Richardson in the 1920s
 118 (Richardson, 1922): the energy is injected at large scales, is cascading in the inertial range
 119 and is dissipated at small scales, smaller than the Kolmogorov scale, which is of the order of
 120 millimeters. The Reynolds number in the atmosphere is in the order of 10^7 to 10^9 , and the
 121 $-5/3$ slope has been found from atmospheric observations by many authors (Sreenivasan &
 122 Antonia, 1997; Calif & Schmitt, 2012; Schmitt & Huang, 2016).

123 The atmosphere is stratified and at very large scales the atmospheric motions seem to
 124 be quasi-two dimensional (Danilov & Gurarie, 2000). This motivated the application of 2D
 125 turbulence phenomenology, as developed by Kraichnan (1967). The phenomenology of 2D
 126 turbulence is very different from 3D turbulence. There is no vortex-stretching term, and the
 127 enstrophy (square of vorticity) can be introduced to propose an enstrophy cascade picture
 128 (Wyngaard, 2010): enstrophy is produced at large scales through mean vorticity gradient,
 129 and is destructed at small scales by viscosity. The enstrophy spectrum has dimensionally a
 130 -1 slope, and since this is k^2 times the energy spectrum, in this range of scales the energy
 131 spectrum follows (Kraichnan, 1967):

$$E_u(k) = C_1 \zeta^{2/3} k^{-3}, \quad k > k_f \quad (2)$$

132 where C_1 is a constant, ζ represents the dissipation rate of enstrophy, and k_f is the wavenum-
 133 ber corresponding to the forcing. At this forcing scale, the enstrophy goes down to small
 134 scales, and the energy has an inverse cascade, going to large scales, with a scaling range as
 135 (Kraichnan, 1967; Vallis, 2017):

$$E_u(k) = C_2 \epsilon^{2/3} k^{-5/3}, \quad k < k_f \quad (3)$$

136 At very large scales, the energy is assumed to be dissipated by friction through Ekman
 137 layers. For the application of this approach to the atmosphere, a quasigeostrophic theory
 138 has been proposed (Charney, 1971), where the enstrophy is replaced by a pseudo potential
 139 enstrophy. In such framework, contrary to Kraichnan's 1967 model, there is a -3 slope at
 140 large scales and a $-5/3$ slope at small scales, for the power spectrum of the velocity field.

141 Finally, let us also mention the 23/9D model proposed by Schertzer and Lovejoy since
 142 the 1980s (Schertzer & Lovejoy, 1985, 1987; Lovejoy et al., 2009). Anisotropic feature
 143 are suggested at all scales with different scaling exponents in the horizontal and vertical
 144 directions, where the former is dominated by the energy flux with a slope of $-5/3$ and the
 145 latter by the buoyancy variance flux with a slope $-11/5$ (Bolgiano, 1959; Obukhov, 1959).
 146 Later, the horizontal anisotropy has been taken into account in the 23/9D model and verified
 147 by using the European Centre for Medium-Range Weather Forecasts (ECMWF) reanalyses
 148 data (Lovejoy & Schertzer, 2011). This model is also discussed and checked in more recent
 149 works (Lovejoy & Schertzer, 2013; Pinel & Lovejoy, 2014). The results show that this model
 150 is capable to explain numerous claims of transition phenomena, for instance the spurious
 151 -2.4 slope for aircraft collected data can be interpreted by the anisotropic 23/9D turbulence
 152 model, rather than the isotropic 3D or 2D turbulence models.

153 2.2 Theories for the Oceanic Waves

154 Under a turbulent wind forcing over the sea, a part of the wind energy is transferred
 155 to the water masses through the surface wind shear. Since the wind forcing, in the inertial
 156 range, has no characteristic scale, and since the related processes involved no obvious char-
 157 acteristic scales, scaling laws for the sea surface height (SSH) have been proposed since the
 158 1950s. They write as:

$$E_\Psi(k) \sim k^{-B} \quad (4)$$

159 where $E_\Psi(k)$ is the Fourier power spectrum of the spatial 2D SSH field, and B is the scaling
 160 exponent. This is valid in a range found over high wavenumbers corresponding to a so-
 161 called equilibrium range involving gravity waves. Such range describes breaking waves have

162 large curvatures, and even nearly discontinuous slopes, with sharp and random crests. By
 163 considering dimensional analysis, one early proposal was Phillips (1985a), who proposed
 164 $B = 4$. This value was also advanced later by Belcher and Vassilicos (1997) using different
 165 dynamical and geometrical arguments: $B = 5 - D$ was proposed. With considering the
 166 balance arguments, a value of the dimension $D = 1$ was found. On the other hand Phillips
 167 (1985b) revoked the $B = 4$ result and proposed $B = 7/2$, for taking into account wave
 168 breaking and wave-wave interactions, and assuming that the nonlinear energy flux, wind
 169 forcing, and dissipation are in balance, proportional, and of comparable magnitude.

170 These results concern about the SSH variable, at small scales, in part smaller than
 171 the scale range spanned by satellites. What is recorded by CFOSAT satellite is Hs, a local
 172 indicator, at the pixel size, of the intensity of the waves. The Hs has been originally defined
 173 as the average of the highest one-third of waves that occur during a given period. Nowadays
 174 it is usually defined as four times the standard deviation of the ocean surface elevation. As
 175 the value of Hs is estimated locally, it may have also spatial variations. However, its relation
 176 with SSH is not direct and there is no theoretical predictions in the literature concerning a
 177 scaling behavior of Hs, either directly or in relation with theoretical proposals for SSH.

178 3 Data and Methods

179 3.1 Data

180 The simultaneously observed WS and Hs data in this study are provided respectively
 181 by a rotating fan beam scatterometer (SCAT) and surface waves investigation and monitor-
 182 ing radar (SWIM), both boarded on CFOSAT. Both instruments use Ku band microwave
 183 frequencies, and SCAT uses medium incidence angles (from 26° to 46°) to retrieve the wind
 184 vectors at 10m height, whereas SWIM operates at near-nadir incidence angles (from 0° to
 185 10°) to retrieve sea-surface waves (Liu et al., 2020). With an orbital repetition cycle of 13
 186 days and accounting for the instrument geometry, which can provide a 1000 km width of
 187 swath for the wind field as illustrated in Figure 1a, the system provides a global coverage
 188 within 3 days for wind fields and nearly global for waves (Hauser et al., 2016).

189 The wind field is not directly measured; it is estimated using a geophysical model
 190 function, which gives the relation between the microwave scattered field, incidence angle,
 191 wind direction and speed close to the sea. Using this approach, an algorithm is designed
 192 to retrieve the 10m wind intensity and direction, from backscattered data from the SCAT
 193 instrument. When the scatterometer has an inclined beam, both wind speed and direction
 194 can be retrieved. This is why rotating beam scatterometers are used since SeaWinds on-
 195 board the satellite QuikSCAT (Spencer et al., 1997). A similar design is used in CFOSAT,
 196 using two fan beams, one vertically polarized, and the other horizontally polarized (Lin &
 197 Dong, 2011; Lin et al., 2018). The processing done involves averaging several backscatter
 198 values having similar incidence and azimuth angles: the larger the number of views, the
 199 more precise results can be obtained. As compared to fixed fan beams or pencil beams
 200 scatterometers, the rotating fan beam system used by SCAT can obtain more observations
 201 of the azimuth angles within a single swath: normally 4–16, more than ten in most areas
 202 for SCAT, while for fixed fan beams or pencil beams, the maximum number is equal to 4
 203 (Zhang et al., 2021). Thus, the wind information retrieval accuracy is greatly increased in
 204 the CFOSAT mission (Liu et al., 2020).

205 For obtaining Hs, an “adaptive retracking” algorithm is performed (Tourain et al.,
 206 2021). The main idea of this algorithm is the following. Different pulses are received by the
 207 satellite sensor, coming from reflections at the ocean’s surface. These different backscattered
 208 echos are classically treated using a model of the ocean’s rough surface (Brown, 1977), seen
 209 as the convolution of a point source, a flat sea surface and an assumed probability density
 210 function of sea elevation. Different improvements of this algorithm have been proposed since,
 211 and a modified version, used for CFOSAT, is described in details in Tourain et al. (2021).

This algorithm is still based on the fit of the Brown model echo (Brown, 1977) to the recorded waveforms and the use of a maximum likelihood estimator. One of the improvements as compared to the conventionally used algorithms for other altimeter missions is the use of the real point target response from the SWIM sensor, instead of a theoretical one. Other improvements are linked with inversion methods using new analytical models.

With all of these improvements, the performance of the CFOSAT mission was found to be remarkable: the accuracy of the Hs is 25 – 30 cm or 5% of the mean value; the accuracy of the wind field is 2 m/s in magnitude and 20° in direction (Suquet et al., 2019; Liu et al., 2020; Hauser et al., 2020; Li et al., 2021).

The WS data used in this study are in a 12.5 km resolution covering the period from December 18, 2018 to August 31, 2020, which is nearly 9200 orbits. For each orbit, the satellite can generate a wind field dataset with a size of 84×3440 pixels. Conventionally, the measured WS is treated as 10 meter wind above the sea surface. In other words, it is still in the marine-atmospheric boundary layer. The Hs data analyzed here were collected from July 29, 2019 to August 31, 2020, which is 7200 orbits with a nominal spatial resolution of 1.5 km. Figure 1a shows an example of the along-track wind field and Hs data collected in the western Pacific Ocean on September 4, 2019 during the Typhoon Lingling (Xu et al., 2019). The corresponding along-track WS and Hs are shown as black and red dots respectively in Figure 1b. The signal of Typhoon Lingling (2019) can be distinguished by the CFOSAT observation, and the typhoon-induced enhancements of WS and Hs are clearly visible. Note that the WS and Hs data used in this paper are Level-2 products, which means the data are processed without any further interpolations. Thus, the original dynamical features of atmosphere and ocean surface can be well preserved in these data.

Before the processing of the data, quality control (QC) was performed. For WS, only the data collected by more than two beams are considered. As for Hs, a Hampel identifier (Davies & Gather, 1993) is chosen to detect the outliers. Hampel identifier uses the median and median absolute deviation as a robust estimate of the location and spread of the outliers. For each data series, firstly a value of W points of the window half-width is given. Then the identifier computes the median of a window composed of the sample and its $2W$ surrounding samples, W data points per side. Besides, the median absolute deviation is also estimated. If a sample differs from the median by more than three times the standard deviations, it is treated as an outlier. This identifier has been proven extremely effective in practice for various fields (Pearson, 2002; Pearson et al., 2015, 2016). In this study, the window half-width is set as 150 data points and the abnormal data are set as Not-a-Number (NaN). As a result, there are roughly 15% of the WS and 2% of the Hs data discarded.

Figure 2 shows an example of the WS and Hs data before and after QC. The black dots represent the raw data provided by the CFOSAT, and the red dots are the data after QC. To minimize the estimation bias for the calculated Fourier power spectrum, a small portion of normal data which successive to the abnormal ones are also excluded in the QC procedure. Figure 3 shows the probability density functions (pdf) of WS and Hs before and after QC, computed over all the data: the pdf tails are cut off after QC. The pdf of WS shows an exponential tail for values larger than 16 m/s. The tail is in the form of $\exp(-x/V_0)$ where the characteristic scale is $V_0 = 1/0.31 = 3.22$ m/s. For Hs data, there is also an exponential form in the ranges of 5 to 15 m: here the tail is in the form of $\exp(-x/L_0)$ where the characteristic scale is $L_0 = 1/0.39 = 2.56$ m.

3.2 Spectra and Co-spectra Estimated via the Wiener-Khinchine Theorem

In this work, the Fourier power spectra $E(\mathbf{k})$ are estimated via the Wiener-Khinchine theorem. More precisely, the Fourier transform of the autocorrelation functions $\rho(\mathbf{r})$ as follows:

$$E_\phi(\mathbf{k}) = \mathcal{R} \int_{-\infty}^{+\infty} \tilde{\rho}(\mathbf{r}) \exp(-j2\pi\mathbf{k}\mathbf{r}) d\mathbf{r}, \quad (5)$$

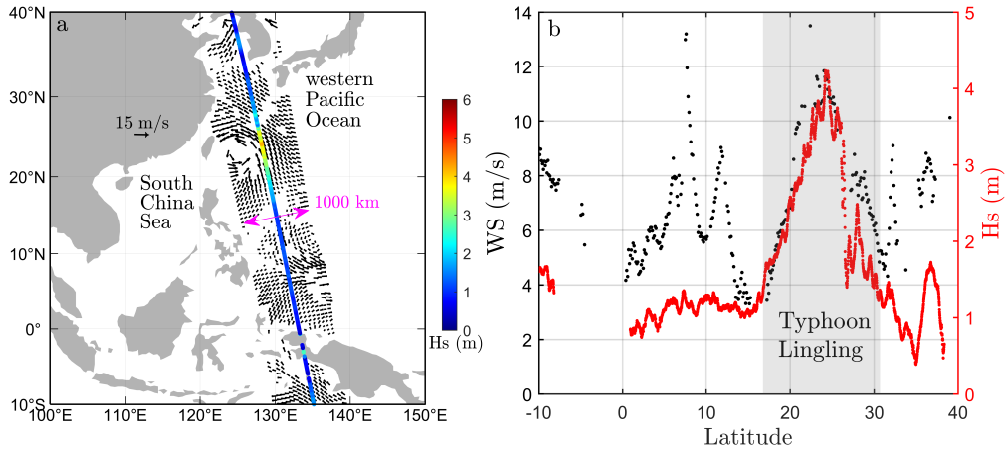


Figure 1. (a) Simultaneously observation of wind vectors (black arrows) and Hs (color dots) by CFOSAT in the western Pacific Ocean on September 4, 2019 during the Typhoon Lingling. (b) The corresponding along-track WS observed by SCAT (black dots) and Hs observed by SWIM (red dots).

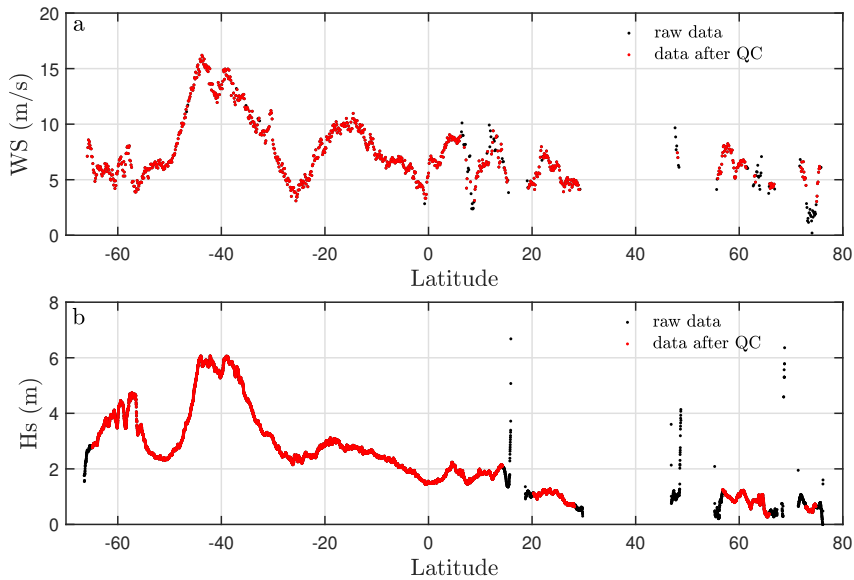


Figure 2. Comparisons of raw data (black dots) and the data after quality control (red dots). (a) and (b) indicate WS and Hs data, respectively.

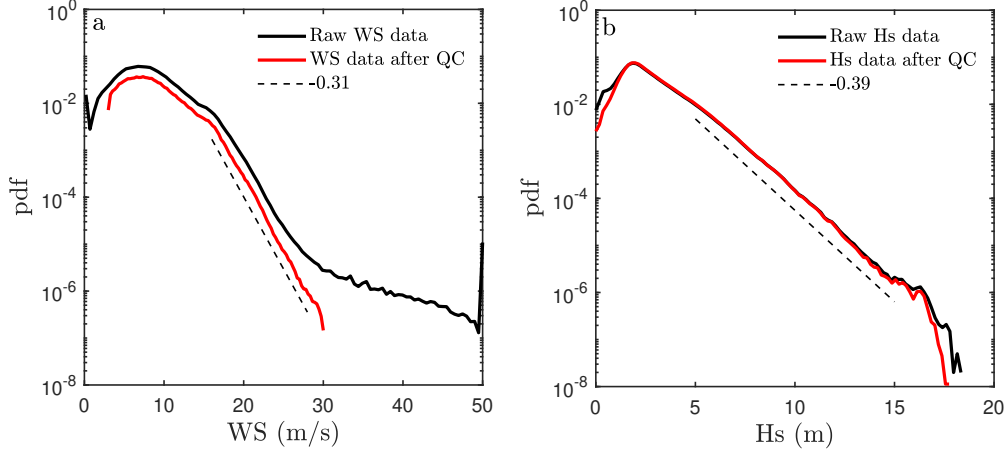


Figure 3. The comparisons of the pdfs of WS and Hs data before (black curves) and after (red curves) QC. Dashed lines emphasize the exponential tails which are found, and the fitted slopes are indicated.

261 in which \mathcal{R} means real part, $j = \sqrt{-1}$ is the complex unit, \mathbf{k} is the wavenumber vector, \mathbf{r} is
 262 the distance vector, and,

$$\tilde{\rho}(\mathbf{r}) = \langle \rho_m(\mathbf{r}) \rangle_m, \quad \rho_m(\mathbf{r}) = \frac{1}{M_m(\mathbf{r})} \sum_{i=1}^{M_m(\mathbf{r})} \tilde{\phi}_m(\mathbf{x}_i + \mathbf{r}) \tilde{\phi}_m(\mathbf{x}_i) \quad (6)$$

263 where $\tilde{\phi}_m(\mathbf{x}_i) = \phi_m(\mathbf{x}_i) - \langle \phi_m(\mathbf{x}_i) \rangle$ is the centered $\phi_m(\mathbf{x}_i)$, ϕ_m is the value of either WS
 264 or Hs of the m th orbit, $\langle \rangle_m$ means spatial average over the m th orbit, and $M_m(\mathbf{r})$ is the
 265 sample size at the separation scale r for the m th orbit. Due to several reasons, such as the
 266 presence of sea ice, lands, bad measurements, the collected WS and Hs data often contain
 267 gaps. The use of the autocorrelation here prevents problems coming from small gaps. To
 268 mitigate the impacts of missing data to the spectral analysis, orbits with the ratio of more
 269 than 50% of the valid data are then accepted. It is found empirically that the averaged
 270 autocorrelation function $\tilde{\rho}(\mathbf{r})$ and the corresponding power spectra $E_\phi(\mathbf{k})$ are not affected
 271 by these missing data. In this work, the radially averaged Fourier power spectrum of the
 272 WS data is also estimated: in such case, the autocorrelation function of the 2D wind field
 273 is estimated; then the 2D power spectrum $E_u(\mathbf{k})$ is calculated via the Wiener-Khinchine
 274 theorem. Assuming a horizontal statistical isotropy, the radially averaged Fourier power
 275 spectrum $E_u(\hat{k})$ is estimated by an angle integration of the 2D spectrum. For a convenient
 276 comparison with the 1D spectrum, the final radially averaged spectrum is multiplied by the
 277 wavenumber modulus $\hat{k} = |\mathbf{k}|$.

278 In case of scaling and isotropy, a power-law behavior of the Fourier spectrum is expected:

$$E_\phi(k) \propto k^{-\beta}, \quad (7)$$

279 where k is one component of the wavenumber vector \mathbf{k} , and β is the so-called scaling expo-
 280 nent, which represents the absolute value of the slope of the best-fit straight line between
 281 $\log(E_\phi(k))$ and $\log(k)$ on a certain range of k values corresponding to the scaling range. Let
 282 us note that the Hs data are scalar, whereas WS data are 2D vectors. In the remaining of
 283 the manuscript, the WS analysis is done on the velocity amplitude, except when zonal and
 284 meridional components of WS are compared: in the latter case each vectorial component is
 285 analyzed separately for comparison.

286 For estimating the co-spectrum for WS and Hs, we perform a similar procedure. The
 287 mean cross-correlation function $\tilde{\rho}_{WS,Hs}(\mathbf{r})$ is estimated. The co-spectrum is then derived

288 from Fourier transform via the Wiener-Khinchine theorem:

$$E_{WS,Hs}(\mathbf{k}) = \mathcal{R} \int_{-\infty}^{+\infty} \tilde{\rho}_{WS,Hs}(\mathbf{r}) \exp(-2j\pi\mathbf{k}\mathbf{r}) d\mathbf{r}. \quad (8)$$

289 3.3 Coherency Spectrum

290 To identify the relation between WS and Hs, the co-spectrum is normalized with the
291 1D spectra for WS and Hs to get the coherency spectrum,

$$H_{WS-Hs}(\mathbf{k}) = \frac{|E_{WS,Hs}(\mathbf{k})|^2}{E_{WS}(\mathbf{k})E_{Hs}(\mathbf{k})}, \quad (9)$$

292 where $0 \leq H_{WS-Hs}(\mathbf{k}) \leq 1$. When the value of coherence function value is equal to 1, there
293 is a perfect linear relationship between the two signals. When the value is 0, then there is
294 no relationship between the two signals (Formenti, 1999).

295 3.4 De-aliasing

296 Another problem often occurring in the Fourier power spectrum analysis is due to alias-
297 ing: when the sampling frequency rate is less than twice the highest frequency of the physical
298 process, namely, the data are undersampled. For undersampled datasets, measurements of
299 their power spectra will often be distorted by aliasing, not only near the Nyquist frequency,
300 but also below it (Kirchner, 2005). To correct the distortions introduced by spectral alias-
301 ing, and recover the spectrum, Kirchner (2005) proposed a filtering method which does not
302 require some *a priori* knowledge of the true spectrum. Here note $E_X(f)$ is the true spec-
303 trum and $E_Y(f)$ is the measured one which includes some degree of aliasing. The formula
304 to derive $E_X(f)$ from $E_Y(f)$ is as follows,

$$E_X(f) = \frac{E_{X_{\text{model}}}(f)}{E_{Y_{\text{model}}}(f)} E_Y(f), \quad (10)$$

305 in which $E_{X_{\text{model}}}(f)$ and $E_{Y_{\text{model}}}(f)$ are model functions defined as

$$E_{X_{\text{model}}}(f) = \frac{E_0 f^{-\alpha}}{1 + (f/f_c)^2} \approx \begin{cases} E_0 f^{-\alpha}, & f \ll f_c \\ E_0 f_c^2 f^{-(\alpha+2)}, & f \gg f_c, \end{cases} \quad (11)$$

306 and

$$E_{Y_{\text{model}}}(f) = E_{X_{\text{model}}}(f) + \sum_{n=1}^{\infty} E_{X_{\text{model}}}(nf_s - f) + E_{X_{\text{model}}}(nf_s + f). \quad (12)$$

307 Here E_0 is an arbitrary constant that sets the scale of the spectral power, f_s is the sampling
308 frequency and f_c indicates the corner frequency, which must typically be specified *a priori*.
309 As long as f_c is substantially above f_s , the exact value of f_c will have little effect on the alias-
310 filtered spectrum. The parameter α is auto determined by a nonlinear fitting procedure,
311 which finds the value of α for which $E_{Y_{\text{model}}}(f)$ matches the measured spectrum $E_Y(f)$
312 as closely as possible. In this way, the effects of aliasing to the spectral analysis can be
313 suppressed.

314 4 Results

315 4.1 Scaling Features at the Global Scale

316 The global averaged spectra of WS (blue curves) and Hs (red curves) are shown in
317 Figure 4. The dotted and solid curves indicate the raw and alias-filtered spectra, respectively.
318 The straight lines are given as references with different slopes. In the high wavenumber
319 ranges, due to the existence of spectral aliasing, the raw spectra exhibit upward trend,
320 mainly visible for WS. After applying the alias-filtered processes, the tails are downward

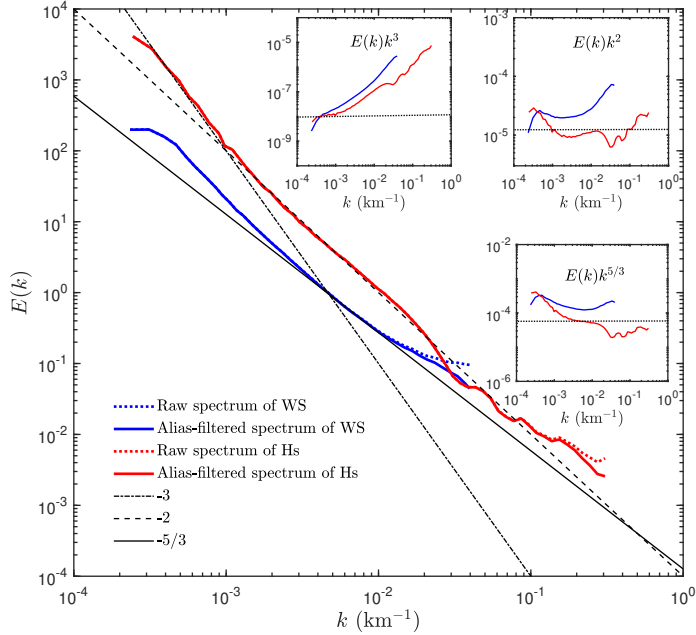


Figure 4. The global averaged Fourier power spectra of WS (blue curves) and Hs (red curves), the dotted and solid line styles mean the raw spectra and the spectra after alias-filtered. The black dash dotted, dashed, and thin lines are given as references with the slopes of -3 , -2 , and $-5/3$. The insets show the corresponding compensated spectra.

321 recovered. In the wavenumber ranging from 1×10^{-3} to 1×10^{-2} km^{-1} , corresponding to
 322 the spatial scales (r) from 100 to 1000 km, the scaling exponent β for Hs is close to 2,
 323 as shown in Figure 4. For wavenumbers smaller than 1×10^{-3} km^{-1} ($r \geq 1000$ km), β
 324 for Hs approaches 3. As for the wavenumbers higher than 1×10^{-2} km^{-1} ($r \leq 100$ km), the
 325 spectrum of Hs illustrates a conspicuous decreasing trend in the spatial scales from 30 to 100
 326 km, then small fluctuations occur along the spectrum. The spectrum of WS also exhibits
 327 power-law features in the range from 100 to 3000 km, and the values of β are between $5/3$
 328 and 3 with small variations. A finer inspection shows that in the range from 100 km to 250
 329 km, the slopes of WS spectra are close to $-5/3$. These multiscale features for WS and Hs
 330 are also emphasized in the compensated spectra as insets.

331 The averaged spectra of zonal and meridional components of WS are also calculated
 332 to tentatively test the horizontal directional isotropy of the wind field. The comparison of
 333 these two spectra is illustrated in Figure 5a. The blue and red curves represent the zonal
 334 and meridional component along track spectra, respectively. These two spectra show similar
 335 scaling features, with the zonal component spectrum slightly larger than the meridional
 336 one, which has been previously reported by Freilich and Chelton (1986). In order to better
 337 compare these two spectra, we introduce their ratio as:

$$I(k_y) = \frac{E_v(k_y)}{E_u(k_y)}, \quad (13)$$

338 where v and k_y are the velocity and the wavenumber components along track. This ratio
 339 is displayed in Figure 5 b. The inset in log-log plot shows a horizontal line, confirming that
 340 zonal and meridional spectra have the same scaling exponent, from 100 to 3000 km. In
 341 turbulence such ratio is called the isotropy ratio and for $5/3$ spectra, in case of isotropy,
 342 the value $I(k_x) = 3/4$ is derived, using symmetry arguments, from the continuity equation
 343 (Kolmogorov, 1941; Monin & Yaglom, 1971).

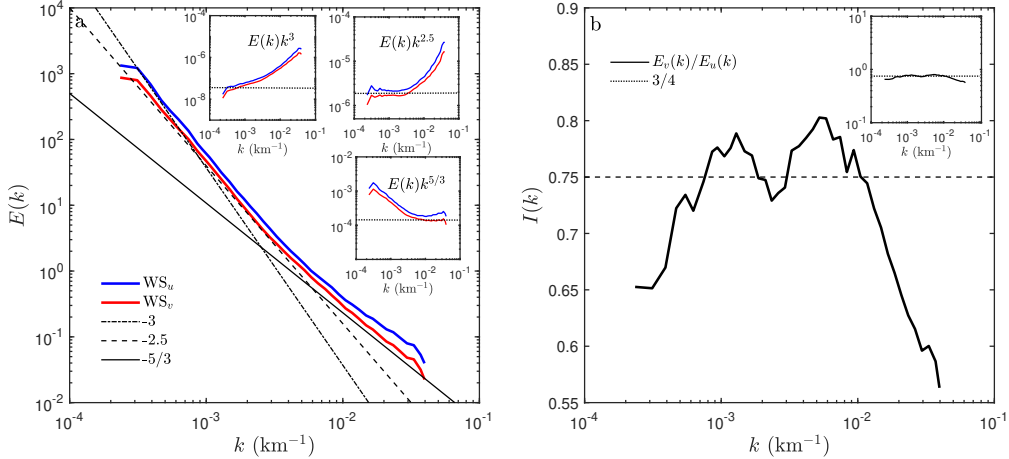


Figure 5. (a) The global averaged Fourier power spectra of zonal (blue curve) and meridional (red curve) components of WS; the black lines are references. The insets show the corresponding compensated spectra. (b) The corresponding isotropy ratio function; the dashed black line indicates the theoretical value $3/4$ expected in case of isotropy (Kolmogorov, 1941); the inset is in log-log plot.

344 To consider the dynamical links between WS and Hs, the co-spectrum $E_{co}(k) =$
 345 $E_{WS,Hs}(k)$ for WS and Hs is estimated and illustrated in Figure 6 a. Power-law features
 346 can be found from the corresponding spatial ranges from 30-250 km and 250-2000 km with
 347 the scaling exponents equal to 1.8 and 2.4, respectively. The compensated spectra as inset
 348 confirm the scaling features. The coherence function $H_{WS-Hs}(k)$ between WS and Hs is
 349 also estimated and shown in Figure 6b, where a log-log plot is shown as inset. The values
 350 of coherence function lie between 0.04 and 0.13 in the whole wavenumber domain, with a
 351 peak value occurring in the separation scale around 1200 km.

352 4.2 Analyses in Basin Scales

353 In order to perform more analyses at smaller portions of the globe, the world ocean
 354 is separated into five regions: the Indian Ocean, the North Atlantic Ocean, the South
 355 Atlantic Ocean, the North Pacific Ocean, and the South Pacific Ocean. This provides
 356 scaling characteristics of WS and Hs spectra in different oceanic areas. The measured
 357 ensemble averaged Fourier power spectra are shown in Figure 7a (WS) and Figure 7b (Hs).
 358 The spectra measured from different ocean basins have all the same shape and share the
 359 same scaling properties.

360 The spectra of WS display a very clear scaling with exponents close to 2, for scales
 361 from 25 to 2500 km, for all basins. Concerning Hs, the scaling exponents β are close to 3,
 362 and 2 for the ranges from 500 to 3000 km and 50 to 500 km, respectively. The compensated
 363 spectra are also given in Figure 7 to emphasize the scaling feature.

364 4.3 Scaling Analysis at Smaller Scales, Below 1000 km

365 In the above analysis, the whole basin as a unit was considered to calculate the spectra
 366 of WS and Hs. The results were nearly identical for different ocean basins. In order to better
 367 characterize the dynamical features of WS and Hs in different oceanic regions, datasets of
 368 finer scale are used to measure the power spectra.

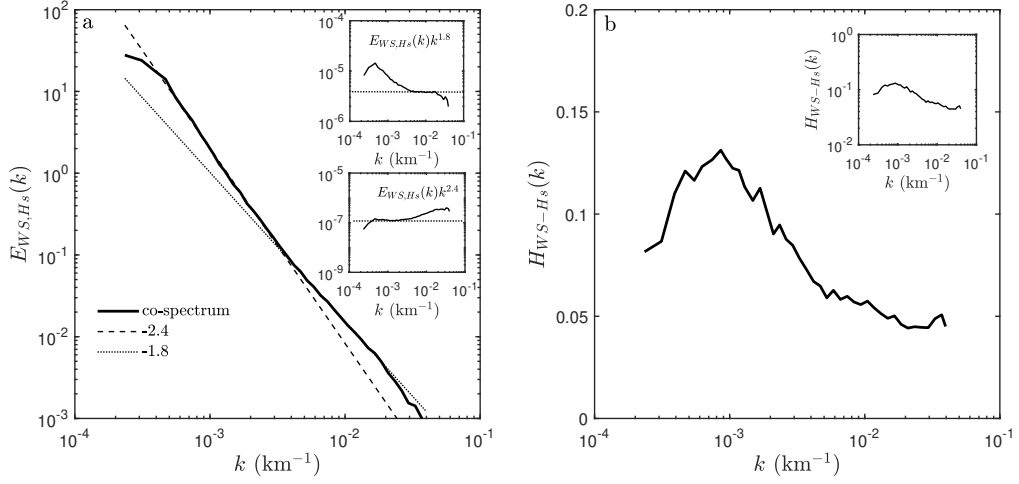


Figure 6. (a) Global averaged cross-spectrum of WS and Hs. The insets show the corresponding compensated spectra. (b) The coherence function between WS and Hs in the semi-log coordinate; the inset is in log-log plot.

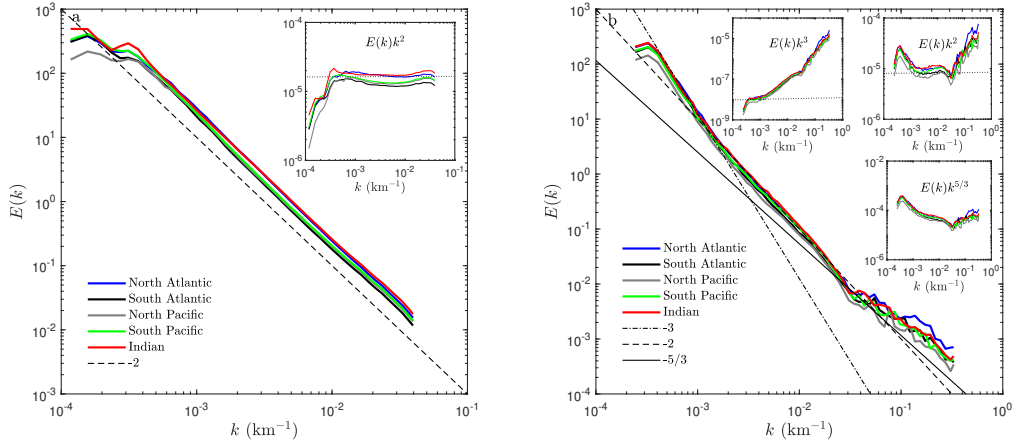


Figure 7. The ensemble averaged Fourier power spectra of the WS (a) and Hs (b) in different oceanic basins; the black dash dotted, dashed and thin lines are given as references. The insets show the corresponding compensated spectra.

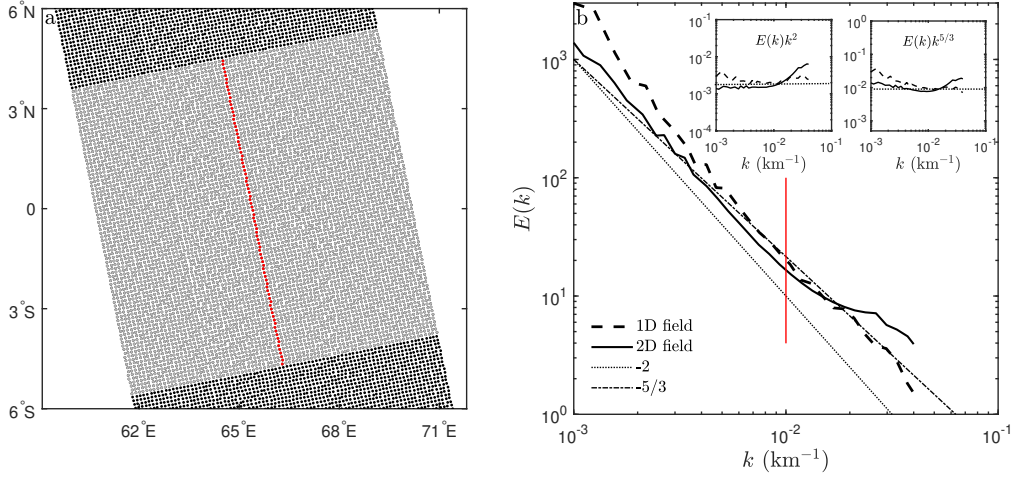


Figure 8. (a) An example of the selected 84×84 2D domain of WS (gray dots); the line formed by red dots indicates the 1D field along the track of the satellite. (b) The global averaged Fourier power spectra measured from the 1D (dashed curve) and 2D (solid curve) WS subsets. The dotted line and dash-dot line are given as references with slopes equal to -2 and $-5/3$, respectively. The insets are the corresponding compensated spectra. The red line in (b) indicates the separation scale of the spectra, to emphasize the chosen scale, 100-1000 km.

369 For WS, the data were separated into 84×84 boxes for each orbit, each one being
 370 approximately a square area with a spatial scale of about $1000 \text{ km} \times 1000 \text{ km}$. Figure 8a
 371 gives an example of a 2D domain, in which the selected subset are shown as gray dots. The
 372 radially averaged Fourier power spectrum is then estimated by the aforementioned algorithm
 373 for the WS magnitude. For comparison, another approach to derive the scaling features for
 374 WS with the scales below 1000 km is to consider the 1D WS data along the satellite track
 375 (red dots in Figure 8a). The global averaged Fourier power spectra for the subsets of WS
 376 in 1D (along the track) and 2D (spatial zone) are illustrated in Figure 8b. Scaling features
 377 are found for both spectra on the scale range of 100-1000 km with a scaling exponent close
 378 to a value of 2, see the compensated curves in the insets.

379 Concerning Hs, 700 along-track data points (which form a total of nearly 1000 km)
 380 are selected as a whole to calculate the spectrum at smaller scales. In this way, the lowest
 381 wavenumber of spectra is around $1 \times 10^{-3} \text{ km}^{-1}$. In order to increase the number of mea-
 382 surements to cover the global ocean, the selected data are overlapped 75% along the satellite
 383 track. Figure 9 illustrates the global averaged Fourier power spectrum for the Hs case. A
 384 scaling feature is distinguished in the range of 10-1000 km, again with a scaling exponent
 385 close to a value of 2.

386 The global distributions of scaling exponents for WS and Hs are derived by averaging
 387 the scaling exponents which are located on the same $2^\circ \times 2^\circ$ grid. This is done for the
 388 scale ranges chosen for each field (e.g., 100-1000 km for WS, and 10-1000 km for Hs). The
 389 results are illustrated in Figure 10 respectively (a) for WS and (b) for HS. The scaling
 390 exponents for WS and Hs both exhibit clear latitudinal dependence. Distinct boundaries
 391 which separate the scaling exponents whose values are larger or smaller than 1.8 are found
 392 around the horse latitudes (30 degrees north and south of the equator) for WS. Moreover, a
 393 small portion with large scaling exponents is found near the equatorial eastern Pacific (e.g.,
 394 roughly 90°W to 160°W and 10°S to 10°N), which coincidentally is in the same region as
 395 the famous Pacific equatorial dry zone (Hastenrath, 1999). For the nearby regions, such
 396 as the Intertropical Convergence Zone (ITCZ), equatorial Pacific Warm Pool (PWP), and

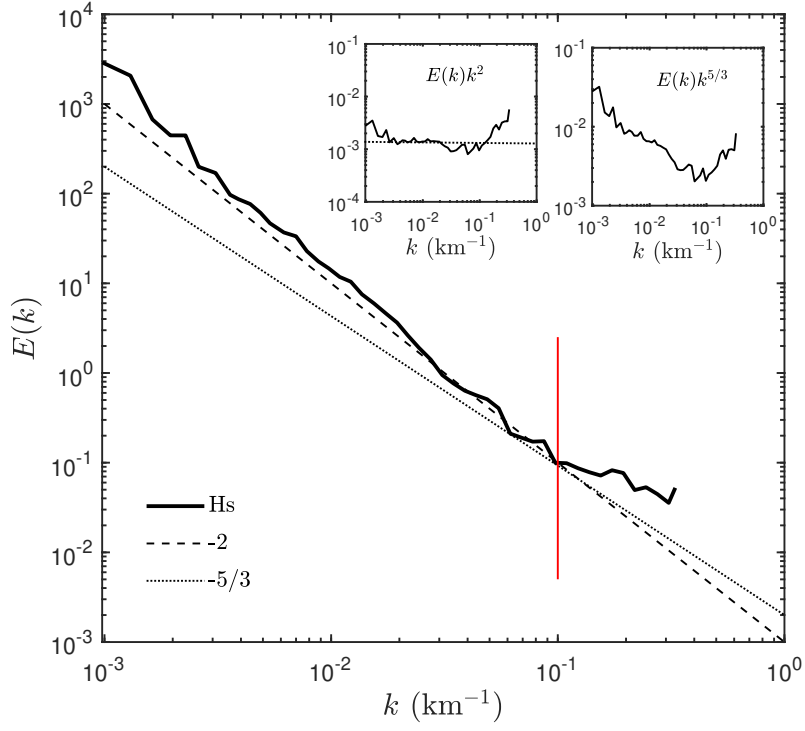


Figure 9. The global averaged Fourier power spectrum measured from the subsets of Hs; the dashed and dotted lines are given as references with slopes of -2 and $-5/3$. The insets are the corresponding compensated spectra. The red line indicates the separation scale of the spectrum to emphasize the chosen range, 10-1000 km.

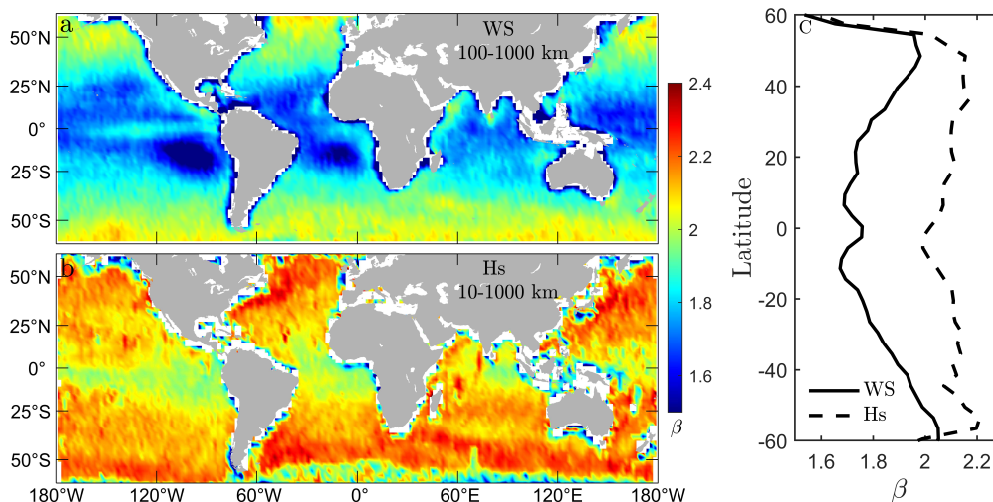


Figure 10. The global distribution of the scaling exponents β measured from (a) WS (100-1000 km) and (b) Hs data (10-1000 km). (c) The meridional variations of β inside the Pacific Ocean. The solid and dashed curves indicate β measured from WS and Hs, respectively.

397 South Atlantic Convergence Zone (SACZ), the scaling exponents for WS are close to $5/3$.
 398 For Hs, the scaling exponents are larger than the ones derived from WS for most regions,
 399 the meridional variations are relatively weak as compare to the WS case. Overall the global
 400 ocean, β for Hs is larger than 2.1 except for the coastal areas. Again, relatively small β is
 401 found in the tropical regions.

402 To quantify the meridional variation of β , a region inside the Pacific Ocean is chosen
 403 (150°E to 100°W , 60°S to 60°N) to perform a meridional average of β . Figure 10 c illustrates
 404 the measured meridional variations of β for WS (solid curve) and Hs (dashed curve). The
 405 variation trends of β for WS and Hs are similar, the maximums occur in mid-latitudes, with
 406 small values in tropical regions. Averaged β derived from WS and Hs are mainly in between
 407 $1.6 - 2.2$ and $1.8 - 2.3$, respectively. A crest value can be found near the equator for WS
 408 case, which corresponds to the Pacific equatorial dry zone mentioned above.

409 Finally, we focus on the seasonal changes of these scaling parameters. For this, the
 410 difference $\Delta\beta = \beta_s - \beta_w$, where β_s is the summer scaling exponent, and β_w the winter one,
 411 is considered. The boreal summer is composed of the months of June, July, and August,
 412 and the boreal winter of the months of December, January, and February. The results are
 413 given in Figure 11. The seasonal variations of β are weaker in mid-latitudes than those
 414 observed in low-latitudes, for both WS and Hs. The scaling exponents for WS are larger
 415 in winter than those in summer for most areas. While for Hs, the seasonal variations of β
 416 are relatively complicated. For Northern Hemisphere, β are larger in summer than those in
 417 winter for most regions; in the tropical area of Southern Hemisphere, β for Hs is larger in
 418 winter, then for the regions further south than 25°S , the seasonal differences are found to
 419 be vaguely.

420 5 Discussion

421 5.1 Wind Data

422 In this work, different scaling laws have been found for the wind velocity data set.
 423 First, the global averaged Fourier power spectrum for CFOSAT observed WS shows power-
 424 law features from 100 to 3000 km where β varies from $5/3$ to 2.5. Figure 5a displaying the

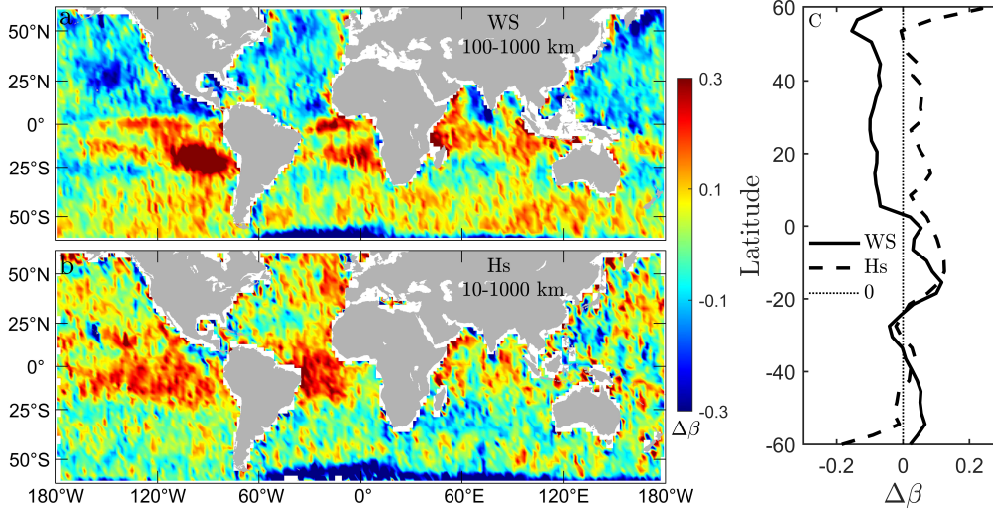


Figure 11. The global distribution of $\Delta\beta = \beta_s - \beta_w$, where β_s is the summer (June, July, and August) scaling exponent and β_w is the winter (December, January, and February) scaling exponent, for (a) WS in the wavelength band of 100-1000 km, and (b) Hs in the wavelength band of 10-1000 km. (c) The meridional variations of $\Delta\beta$ inside the Pacific Ocean. The solid and dashed curves indicate $\Delta\beta$ measured from WS and Hs, respectively.

425 global averaged Fourier spectra of zonal and meridional components of the wind field, shows
 426 that horizontally the wind field is roughly directionally isotropic, since the two curves follow
 427 the same laws as indicated by the insets. The scaling exponents are close to -2.5 for scales
 428 from 300 to 3000 km, and close to $-5/3$ for smaller scales, from 30 to 300 km, corresponding
 429 roughly to the mesoscale.

430 The fact that the meridional spectrum is slightly below the zonal spectrum is due
 431 to symmetry reasons. Indeed, this ratio is $3/4$ for $5/3$ isotropic turbulence, and it is a
 432 constant of the form $I(k) = 2/(1 + \beta)$ for isotropic turbulence with spectral slope β (Monin
 433 & Yaglom, 1971). This ratio is displayed in Figure 5 b: it is close to $3/4$ for some range of
 434 scales for which there is no $5/3$ spectrum. Hence, the value found here is not a proof of
 435 horizontal symmetry, since for the scales for which an approximate $5/3$ slope is found (the
 436 larger wave numbers), the ratio is decreasing. This may be due to the fact that these spectra
 437 are not perfectly scaling. However, this ratio in log-log plot (inset of Figure 5 b) still shows
 438 that there is no clear scaling difference between both spectra: the wind field data appear to
 439 be nearly directionally isotropic on the horizontal plane.

440 Note that previous studies have shown that the atmospheric movements could be
 441 anisotropic with different scaling exponents estimated along meridional, zonal, and vertical
 442 directions (Lovejoy et al., 2007, 2009; Pinel et al., 2014). For example, using the
 443 ECMWF reanalyses data, Lovejoy and Schertzer (2011) found horizontal anisotropy at 700
 444 mbar, corresponding to the top of clouds. As aforementioned, the 10-meter wind field is in
 445 the marine-atmosphere boundary layer, where the horizontal directional isotropy might be
 446 restored due to the interaction with sea surface.

447 At the global scale, different regimes, climates, boundary conditions are mixed. The
 448 basin scale analysis is a way to avoid mixing signals from different zones, especially tropical
 449 zone which provides specific scaling properties. This is why the basin scale analyses show
 450 different results from the global analysis (Figure 4 versus Figure 7). Indeed at the basin scale

451 there is a very neat power-law, from 25 to 2500 km, with a scale ratio of 2 decades. Each
 452 basin shows the same universal property, which is quite remarkable.

453 To have results at finer scales, the analysis has been performed over shorter segments,
 454 over the range from 100 to 1000 km. Globally the estimated β displays patterns emphasizing
 455 the tropical regions, and latitude dependence. This latitude dependence could best be
 456 considered in the Pacific Ocean (Figure 10c), the differences in the value of β are more
 457 marked at high latitudes. Such patterns show the climatic influences on wind scaling regimes.

458 Globally, no scaling range with k^{-3} has been found here. It does not seem to sustain the
 459 enstrophy cascades corresponding to the quasigeostrophic theoretical framework. We find a
 460 $k^{-5/3}$ range, at mesoscales from 25 to 300 km (Figure 5a), followed by an empirical fit close
 461 to the slope of -2.5 for larger scales, from 300 to 3000 km, having no theoretical explanation.
 462 The more detailed analyses (Figure 10) show that the scaling exponents are not so universal
 463 and depend on the location. Strong patterns in this figure illustrate spatial variations of
 464 scaling features associated with different types of climate. Quite often in tropical regions,
 465 the exponents are close to $5/3$, whereas they are between 1.8 and 2.2 for the other areas
 466 (see also Figure 10c).

467 The -2 slopes that are found in the oceanic basins are in agreement with none of the
 468 theories discussed above. It was in fact already found in previous studies using satellite data.
 469 For instance, Freilich and Chelton (1986) examined the Seasat-A satellite scatterometer ob-
 470 served wind vector data over the Pacific Ocean, and found an energy spectrum proportional
 471 to k^{-2} in the range of 200 to 2200 km. Pinardi and Milliff (2004) found also a k^{-2} slope
 472 for the spectrum of the Mediterranean surface winds from QuikSCAT for spatial scales be-
 473 tween 200 km and 1000 km. Chelton et al. (2006) studied the wavenumber spectra of the
 474 QuikSCAT zonal and meridional wind components and the wind speed in the North Pacific.
 475 The results shown that the dependence on wavenumber k for these three variables are all
 476 approximately k^{-2} for scales below 1000 km.

477 We may compare our results with other previous studies. Wikle et al. (1999) considered
 478 wind data from three different sources (e.g., reanalysis wind data from National Centers for
 479 Environmental Prediction, satellite-based ERS-1 scatterometer observed wind, and wind
 480 from high-resolution aircraft observations). They found that the combined spectra from
 481 these data demonstrate a power-law relation over the range 1-1000 km, with a best-fit slope
 482 close to the value of $-5/3$, and the energy spectra for subsets of the data support spectral
 483 slopes of $-5/3$ and -2 . Patoux and Brown (2001) investigated the spectra of QuikSCAT
 484 observed wind vectors. They fitted the spectra on the range of 100-1000 km to derive
 485 the scaling exponents. The values of measured β were roughly between $5/3$ and 3, with
 486 wide variations from 1.8 to 2.6. Then the spatial and seasonal variations of the spectra
 487 slopes were examined. They found that the energy spectra were steeper in midlatitudes,
 488 and all the more so in winter, also with steeper slopes in the tropics in the presence of
 489 convection. They concluded that when convection is enhanced, the energy level is raised at
 490 all scales. Consequently, the energy spectrum is steeper. The seasonal variations correspond
 491 to enhanced baroclinic activities in winter in the midlatitudes. According to our results, in
 492 the strong convection regions, e.g., ITCZ, PWP, and SACZ, the measured β in 100-1000 km
 493 scales is close to $5/3$. The corresponding spectra are flatter than the ones in nearby regions,
 494 i.e., equatorial dry zone with relatively steady atmospheric movements. Xu et al. (2011)
 495 performed a spectral analysis of QuikSCAT winds over the global ocean, and found that β
 496 possesses spatial variability in the scale range of 1000-3000 km, with values varying from 1.6
 497 to 2.9. The slopes of spectra were observed to become steeper toward high-latitudes in the
 498 Pacific and in the South Atlantic. Besides, the spectra are steeper in winter than those in
 499 summer for most regions of the Northern Hemisphere midlatitude. This was also explained
 500 by the baroclinic argument. Furthermore, the seasonal differences which are observed in
 501 our analysis might also be related to the temporal variations of the baroclinic instability
 502 strength.

503 Globally, the analysis for WS subsets found in the present study is relatively consistent
 504 with the results reported by Patoux and Brown (2001) and Xu et al. (2011). With the same
 505 fitting range set as Patoux and Brown (2001), we found β for WS subsets various from 1.6
 506 to 2.2 for most regions, and β are larger in midlatitudes than those in tropics. The regions
 507 in same latitudes but with strong convection show β close to $5/3$.

508 Let us mention some limitations or specific properties of CFOSAT data used in this
 509 study. The wind speed retrieved by the SCAT sensor is typically treated as 10 meters above
 510 the sea surface. This height is close to the bottom of the marine atmospheric boundary
 511 layer, which is often in the order of $\mathcal{O}(1)$ km (Lang et al., 2018). The 10-meter wind is thus
 512 strongly influenced by the bottom conditions, e.g., the effective roughness/wave height,
 513 temperature profiles, the variation of boundary layer, to name a few. Hence, it is not purely
 514 large-scale turbulence and boundary conditions may have influence on the statistics. For
 515 the same reason, one cannot fully compare the results from this sensor to the one of the
 516 altitude measurements using the commercial aircraft, such as the one obtained by Nastrom
 517 and Gage (1985) or other similar measurements done at the height $\mathcal{O}(10)$ km.

518 5.2 Wave Data

519 From global analysis, features for Hs are found in the ranges of 10 to 1000 km and
 520 1000 to 3000 km with β close to 2 and 3, respectively. Some heave and roll features that
 521 occur in the spectrum range below 50 km may be the signature of energy injections induced
 522 by some energetic submesoscale processes, such as eddies and fronts or other interactions
 523 between surface currents, closely related to the upper ocean dynamics, thermodynamics, and
 524 biogeochemistry. At the basin scale, spectra for Hs in different oceanic basins are identical
 525 in the spatial ranges of 50 to 2000 km (Figure 7). As indicated above, there is no theory to
 526 explain such results. We may only compare these findings with previous published works.
 527 Similar studies estimating the spectra for satellite collected Hs were performed by Monaldo
 528 (1988, 1990), where 100 Geosat radar altimeter sampled Hs trajectories around the world
 529 were used to calculate the energy spectra. The scaling exponents were found to be around
 530 1.4 in the spatial scale from several kilometers to about 50 km. Similar scaling features are
 531 observed in our study at small scales (Figure 4 and Figure 7b) where both global and basin
 532 scale averaged spectra are shown. For the scales less than 50 km, the scaling exponents are
 533 slightly smaller than $3/5$. Tournadre (1993) estimated the energy spectra with 583 and 689
 534 Geosat observed Hs trajectories. The corresponding scaling exponents were derived in the
 535 range 14 to 1400 km with the values equal to 1.39 and 1.21, in the North Sea and equatorial
 536 Atlantic respectively. Spatial differences are found, and values of β are larger in midlatitudes
 537 than those in tropics, which is similar to what we found of the spatial distribution of β in
 538 the scale of 10-1000 km, while in our results the slopes are steeper.

539 The parameter Hs is a measure of the local roughness, proportional to the small-scale
 540 variance of the wave field. This quantity shows a scale-dependent variability, with long-range
 541 correlations as revealed by the scaling regimes which have been found. Such properties of Hs
 542 are certainly inherited from the surface wave height field, for which several scaling theories
 543 have been proposed in the literature, as was discussed in a previous section.

544 5.3 Coupling between Wind and Waves

545 Wind and waves are closely related to each other, and the relationship between WS
 546 and Hs has been studied for a long time (Kinsman, 1965; Carter, 1982; Andreas & Wang,
 547 2007; Khandekar, 2013). Due to the limitation of data available, the dynamic features
 548 between WS and Hs in the spatial domain are rarely reported in literature. Bhandari and
 549 Shaeb (2014) examined the spatial coherence of WS and Hs over the Arabian Sea with auto-
 550 correlation functions. They found that the spatial coherence scales are of the order of 100 to
 551 500 km. The Hs and WS data they used were all provided by Poseidon-2 Radar Altimeter.
 552 The WS could have been retrieved from altimeter, but the accuracy is relatively poor as

553 compared to the ones got from scattermeter (Monaldo, 1988; Hwang et al., 1998; Ribal &
 554 Young, 2019). In our study, based on the SCAT observed WS and SWIM collected Hs, the
 555 co-spectrum of WS and Hs was derived at a global scale. Scaling features were found in
 556 the spatial ranges from 30 to 250 km and 250 to 2000 km with scaling exponents equal to
 557 1.8 and 2.4, respectively. Further, the coherence function also illustrated scale dependent
 558 features. These results confirmed the existence of spatially coupled dynamical links between
 559 WS and Hs, and the fact that the mechanisms of these links are related to the spatial scales.
 560 However, the fundamental rules of the interactions between WS and Hs are still unclear and
 561 will be the topic of further works.

562 6 Conclusion

563 Simultaneously observed wind and wave data by CFOSAT have been used to determine
 564 the multiscale features of WS and Hs. Before processing the data, quality controls have
 565 been carefully performed and outliers were removed, as shown by the pdfs of the two main
 566 variables considered here. The spatial and temporal variations of the corresponding scaling
 567 exponents have been examined. Power-law features were found in the global averaged Fourier
 568 power spectra of WS and Hs. The scaling exponents β for Hs are close to 3, and 2 in the
 569 range of 1000-3000 km and 10-1000 km, respectively. For WS, power-law features are found
 570 from 100 to 1000 km with β between $5/3$ and 2, with little evidence of β close to 3 for larger
 571 scales. The global averaged co-spectrum for WS and Hs also showed power-law features
 572 from 30 km to 250 km and 250 km to 2000 km with scaling exponents equal to 1.8 and 2.4,
 573 respectively. The values of the coherence function lay between 0.04 and 0.13 in the whole
 574 spatial ranges, and the maximum occurs around at 1200 km.

575 Our results showed that within each oceanic basin, the averaged Fourier power spectra
 576 for WS and Hs have nearly identical shapes and scaling features from 50 km to 3000 km,
 577 while for the scales below 50 km, the spectra for Hs show more roughness as compared to
 578 those at larger scales. This may indicate that complex submesoscale processes are dominant
 579 at these scales.

580 A finer examination of the global distribution of β showed that the scaling exponents
 581 for WS and Hs are both meridional dependent with large values occurring in middle and
 582 high latitudes and small values in the tropics. For WS, the scaling exponents are smaller
 583 inside the convergence zones than those in the relatively steady equatorial dry zone. The
 584 scaling exponents in convective regions are close to $5/3$. We also considered the temporal
 585 evolution of scaling exponents. Their seasonal variations derived from WS data showed
 586 small scaling exponents in summer and large ones in winter for most regions. This result is
 587 likely related to the strength of baroclinic disturbances in different seasons. While for Hs
 588 case, β are found larger in summer than those in winter in the Northern Hemisphere; in the
 589 tropical area of Southern Hemisphere, large β is found in winter, as for the regions further
 590 south than 25°S , the seasonal variations are unclear.

591 Globally these results show that some scaling properties may be obtained when con-
 592 sidering all the data together, some universal properties are found when considering the
 593 averages in some subsamples, such as the basin scale study, especially for the wind field
 594 when a very clear k^{-2} range was found over 2 decades in scale. The variability of the field
 595 considered, and hence their spectral properties, vary in time and in space and some ade-
 596 quate spatial or temporal domain must be chosen to find evolution, universality, patterns
 597 and identify hidden processes. This is what has been done in this work, either by looking at
 598 the basin scale, the local spatial patterns, the latitude averages in one ocean, or the seasonal
 599 changes in some spatial patterns.

600 In this work, some basic scaling features of WS and Hs collected by CFOSAT have
 601 been derived by spectral analysis. For further works, we plan to characterize also the
 602 intermittency in these scaling ranges, by considering structure functions, joint structure

603 functions and also Hilbert spectral analysis (HSA) of higher orders, which are shown not to
604 be strongly impacted by energetic forcing (Huang et al., 2008, 2011; Schmitt & Huang, 2016).
605 Also, the information provided by one satellite with a single scaling analysis approach is not
606 enough to further diagnose the multiscale dynamical features of WS and Hs. Studies of WS
607 and Hs data from other satellites or in-situ observations with other compensatory scaling
608 analysis methods are needed. Finally, it is planned also to focus more on the dynamical
609 relationships between WS and Hs.

610 **Acknowledgments**

611 The suggestions by two reviewers, that lead to substantial improvements, are acknowl-
612 edged. This work was supported by the CNES (French space agency). It is based on
613 observations with SCAT and SWIM embarked on CFOSAT China-France satellite. This
614 work was supported by the National Natural Science Foundation of China (NSFC) (Grant
615 Nos. 91958203 and 11732010). This research has been performed in the frame of the Mul-
616 tiW2 project, funded by the CNES/TOSCA program. Funding of YG's Cotutella doctoral
617 research project by Région Hauts-de-France and Xiamen University is acknowledged. The
618 CNRS-NSFC project TURBLOOMS (Turbulence and marine algal blooms : use of satellite
619 remote detection; 2019-2021) is acknowledged for partial financial support. YX is partially
620 supported by State Key Laboratory of Ocean Engineering (Shanghai Jiao Tong Univer-
621 sity) (Grant No. 1910). The CFOSAT data used in this study can be freely accessed at
622 <https://www.avisio.altimetry.fr>. The Matlab and Python codes are freely available at
623 <https://github.com/lanlankai>. The authors are grateful to the team of China France
624 Oceanography Satellite.

625

Appendix A CFOSAT Orbits

626

In the main text, we mentioned that the CFOSAT provides a global coverage every roughly 3 days for both the wind field and waves. The CFOSAT orbit is fixed: it cannot provide a 24-hour observation for the same region, see Figure A1.

628

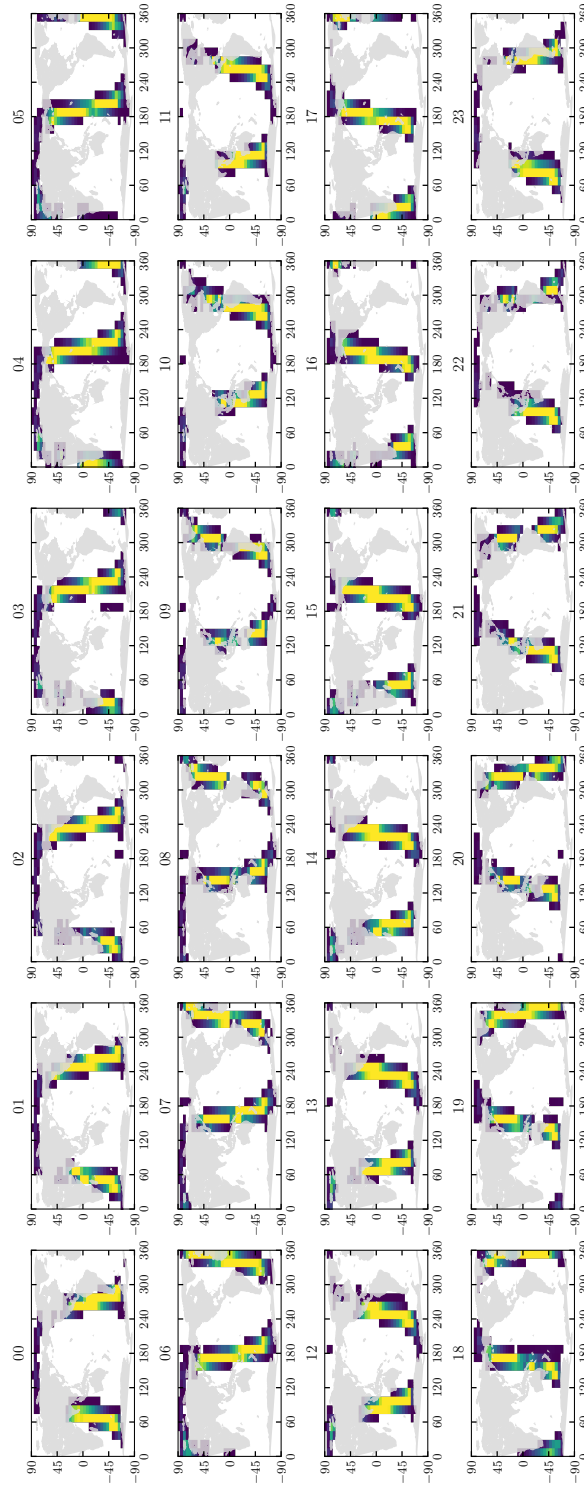


Figure A1. The data distribution at different times. The CFOSAT orbit is fixed.

629

Appendix B Effect of outliers on β

630

631

632

633

634

635

636

637

638

639

Here, we present the effect of outliers on the slope of spectra, by subtracting the measured β with raw data from the ones estimated with data after quality control (QC). The results are illustrated in Figure B1. There are clear spatial variations for both WS and Hs. For WS, the existence of abnormal values leads to flatter spectra in tropical areas (except in ITCZ). While for the other higher latitudes, the outliers make the spectra relatively steep as compared to the ones measured with the data after QC. The differences are all in between -0.2 to 0.2. For Hs, the influence of outliers is mainly found along the coastal and equatorial regions, where the slopes of the spectra are greatly reduced. For the other regions (open oceans), SWIM performs well in Hs observation, since there are relatively small estimation errors. Thus, the differences of β in the open oceans are close to 0 for most regions.

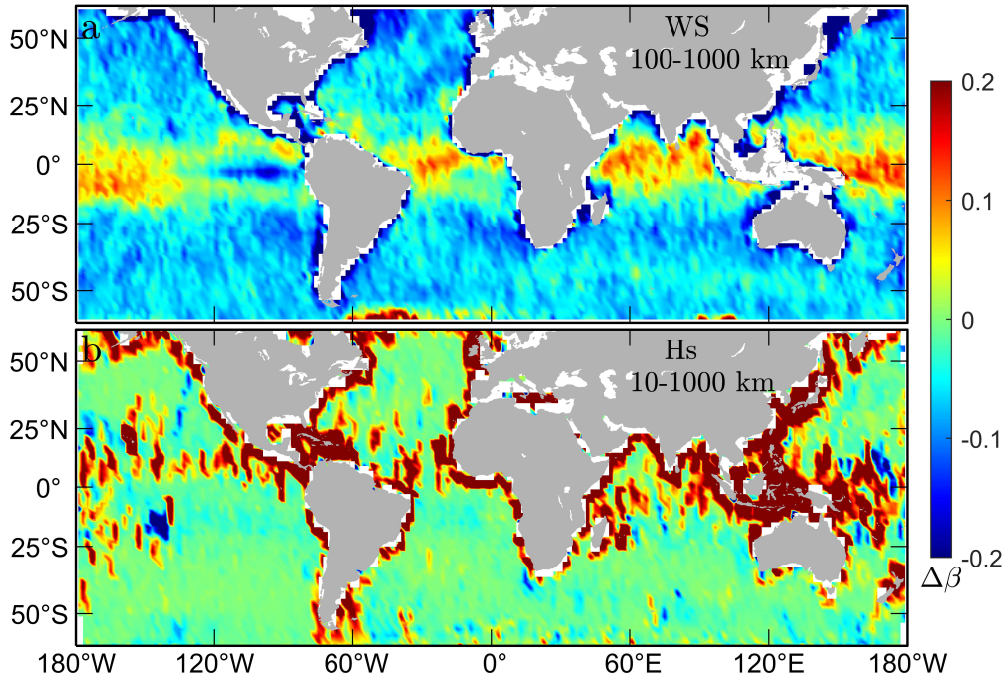


Figure B1. The global distribution of $\Delta\beta = \beta_Q - \beta_R$, where β_Q and β_R are the scaling exponents estimated with data after QC and raw data, respectively. For (a) WS in the wavelength band of 100-1000 km, and (b) Hs in the wavelength band of 10-1000 km.

640 **Appendix C Code for Quality Control**

641 Matlab version codes to perform the quality control is provided below, see Figure C1.
 642 Both Matlab and Python codes are also freely available at: <https://github.com/lanlankai>.

Here is the Matlab code used to remove the outliers in Hs dataset.

```

re_out.m
% This function is used to remove Hs outliers based on Hampel identifier
% x means the raw data
% k means the window half-width
1  function x2=re_out(x,k)
2    [x2,j]=hampel(x,k);
3    x2(j)=nan;
4    lx=length(x);
5    iLo=[1:lx]-k;
6    iHi=[1:lx]+k;
7    iLo(iLo<=0)=1;
8    iHi(iHi>=lx)=lx;
9    xra=zeros(lx,1)*nan;
10   for i = 1 : lx
11     w=x(iLo(i):iHi(i));
12     ind=find(isnan(w)==1);
13     xra(i)=length(ind)/length(w);
14   end
15   ind=find(xra>0.9);
16   x2(ind)=nan;
17   ind2=find(x<0.1);
18   x2(ind2)=nan;
19   end
  
```

Figure C1. A Matlab code to remove the outliers.

643 **Appendix D Code for the Wiener-Khinchine Theorem Preserved Fourier**
644 **Power Spectrum**

645 Matlab version codes to estimate the Fourier power spectrum via the Wiener-Khinchine
646 Theorem (WKT) for both 1D and 2D cases are provided below, see Figure D1, D2 and D3.
647 Both Matlab and Python codes are also freely available at: <https://github.com/lanlankai>.

Matlab version codes to estimate the autocorrelation function for both 1D and 2D data via Wiener-Kinchin theorem (WKT). The missing data is replaced by NaN.

```

fastacf1D.m
%This code is used to estimate the autocorrelation function for 1D data, where the missing
data is replaced by the NaN.
% x means the input data
1 function c=fastacf1D(x)
2   x=x-nanmean(x);
3   Nx=length(x);
4   y=ones(size(x));
5   xi=find(isnan(x)==1);
6   x(xi)=0;
7   y(xi)=0;
8   xf=rfft(x, 2.^(ceil(log2(2*Nx-1))));
9   c1=irfft(abs(xf).^2);
10  c1=real(c1);
11  xf=rfft(y,L);
12  c2=irfft(abs(xf).^2);
13  c2=real(c2);
14  c2=fix(c2);
15  c2(c2==0)=1;
16  c3=zeros(size(c1));
17  c3(1:Nx)=Nx:-1:1;
18  c3(end-Nx+1:end)=c3(Nx:-1:1);
19  c=c1./c2.*c3;
20 end

```

fastacf2D.m
 %This code is used to estimate the autocorrelation function for 2D data via the WKT. The missing data is replaced by NaN.
 %x means the input data

```

1 function c=fastacf2D(x)
2   x=x-nanmean(x,:);
3   ind=find(isnan(x)==1);
4   x(ind)=0;
5   [M,N]=size(x);
6   y=ones(size(x));
7   y_new=y;
8   y(ind)=0;
9   X = fft2(x,2^nextpow2(2*M-1),2^nextpow2(2*N-1));
10  c1 = ifft2(abs(X).^2);
11  c1(M-1:end-M+2,N-1:end-N+2)=0;
12  X = fft2(y,2^nextpow2(2*M-1),2^nextpow2(2*N-1));
13  c2 = ifft2(abs(X).^2);
14  c2=real(c2);
15  c2=fix(c2);
16  c2(c2==0)=1;
17  X = fft2(y_new,2^nextpow2(2*M-1),2^nextpow2(2*N-1));
18  c3 = ifft2(abs(X).^2);
19  c3=real(c3);
20  c3=fix(c3);
21  c=c1./c2.*c3;
22 end

```

Figure D1 shows the Matlab code for estimating the autocorrelation function (ACF) for 1D and 2D data using the Wiener-Kinchin theorem (WKT). The code includes comments and annotations explaining the steps: removing the mean value from the input data, finding the index of NaN, replacing NaN by zeros, calculating the ACF via WKT with zero-padding, determining the number of pairs of valid samples, and finally calculating the ACF with missing data correction.

Figure D1. A Matlab code to estimate the auto-correlation function in both 1D and 2D with the missing data correction.

648

References

649

Andreas, E. L., & Wang, S. (2007). Predicting significant wave height off the northeast

This code is used to estimate the Fourier power spectrum via the autocorrelation function for 1D case

```

acf2psd1D.m
%x means the 1D autocorrelation function
%fs is the sampling frequency
% pd is the estimated power spectrum
%f is the frequency
% bpd is the bin averaged power spectrum in a logarithmic scale
% bin is the corresponding bin
1 function [pd,f,bpd,bin]=acf2psd1D(x,fs)
2   if nargin==1
3     fs=1;
4   end
5   pd=abs(real(ifft(x)));
6   M=length(x);
7   pd=pd(2:fix(M/2));
8   f=[2:fix(M/2)]/M;
9   bpd0=binaverageM(f,pd,20);
10  xi=find(isnan(bpd0.d)==0);
11  bpd=bpd0.d(xi);
12  bin=bpd0.bb(xi);
13  f=f*fs;
14  bin=bin*fs;
15 end

binaverageM.m
%bin average in a logarithmic scale with bq bins each decade
1 function bpd=binaverageM(x,y,bq)
2   if nargin~=3
3     error('Three inputs are required');
4   end
5   dx=1/bq;
6   bin=-dx+log10(min(x)):dx:log10(max(x))+dx;
7   NB=length(bin);
8   bb=zeros(1,NB-1)*nan;
9   bd=zeros(1,NB-1)*nan;
10  x1=log10(x);
11  for i=1:NB-1
12    xi=find(x>bin(i) & x<bin(i+1));
13    if isempty(xi)==0
14      bd(i)=nanmean(y(xi));
15      bb(i)=nanmean(x1(xi));
16    end
17  end
18  bpd.d=bd;
19  bpd.bb=bb;
20 end

```

Diagram annotations for Figure D2:

- Line 3: `fs=1;` → sampling frequency
- Lines 5-7: `pd=abs(real(ifft(x)));`, `M=length(x);`, `pd=pd(2:fix(M/2));` → FPS via WKT, only half of the spectrum is needed
- Line 8: `f=[2:fix(M/2)]/M;` → frequency or wavenumber
- Line 9: `bpd0=binaverageM(f,pd,20);` → bin average of the spectrum with 20 points each bin
- Line 10: `xi=find(isnan(bpd0.d)==0);` → prepare output: the bin without value is excluded
- Line 6: `bin=-dx+log10(min(x)):dx:log10(max(x))+dx;` → prepare the bin in a logarithmic scale
- Line 10: `x1=log10(x);` → logarithm of frequency or wavenumber
- Lines 12-15: `xi=find(x>bin(i) & x<bin(i+1));`, `if isempty(xi)==0`, `bd(i)=nanmean(y(xi));`, `bb(i)=nanmean(x1(xi));` → loop for the bin average
- Line 18: `bpd.d=bd;`, `bpd.bb=bb;` → prepare output

Figure D2. A Matlab code to estimate the 1D Fourier power spectrum and to perform a bin average in a log-scale.

- 650 coast of the United States. *Ocean Engineering*, 34(8-9), 1328–1335.
- 651 Babanin, A. (2006). On a wave-induced turbulence and a wave-mixed upper ocean layer.
- 652 *Geophysical Research Letters*, 33(20), L20605.
- 653 Belcher, S., & Vassilicos, J. (1997). Breaking waves and the equilibrium range of wind-wave.
- 654 *Journal of Fluid Mechanics*, 342, 377–401.
- 655 Bhandari, S., & Shaeb, K. H. B. (2014). Spatial Coherence of winds and waves over the

```

This code is used to estimate the Fourier power spectrum via the autocorrelation function
for 2D case

acf2psd2D.m
%x means the 2D correlation function
%fs is the sampling frequency
% pd is the estimated 2D power spectrum
%pdr is the estimated radially averaged power spectrum
%f is the frequency
% bpd is the bin averaged power spectrum in a logarithmic scale
% bin is the corresponding bin
1 function [pd,pdr,f,bpd,bin]=acf2psd2D(x,fs)
2   if nargin==1
3     fs=1;
4   end
5   pd=abs(real(iff2(x)));
6   pd=fftshift(pd);
7   [M,N]=size(x);
8   pdr = zeros(1, ceil(sqrt((M/2)^2+(N/2)^2)));
9   co = pdr;
10  midx = M/2 + 1;
11  midy = N/2 + 1;
12  for i = 1 : M
13    for j = 1 : N
14      dr = round(sqrt((j - midy)^2 + (i - midx)^2));
15      if dr == 0
16        continue;
17      end
18      pdr(dr) = pdr(dr) + pd(j, i);
19      co(dr) = co(dr) + 1;
20    end
21  end
22  co(co==0)=1
23  pdr = pdr ./ co;
24  pdr=pdr(2:end-1);
25  f=2:length(pdr)+1;
26  f=f/length(pdr)/2;
27  bpd0=binaverageM(f,pdr,20);
28  xi=find(isnan(bpd0.d)==0);
29  bpd=bpd0.d(xi);
30  bin=bpd0.bb(xi);
31  f=f*fs;
32  bin=bin*fs;
33 end

```

Diagram annotations for Figure D3:

- Line 3: `fs=1;` points to a box labeled "sampling frequency".
- Lines 5-6: `pd=abs(real(iff2(x)));` and `pd=fftshift(pd);` are grouped by a bracket pointing to a box labeled "2D FPS via WKT".
- Lines 8-11: `pdr = zeros(1, ceil(sqrt((M/2)^2+(N/2)^2));`, `co = pdr;`, `midx = M/2 + 1;`, and `midy = N/2 + 1;` are grouped by a bracket pointing to a box labeled "prepare for radially averaged FPS".
- Lines 12-21: The nested `for` loops and the `pdr` and `co` update lines are grouped by a bracket pointing to a box labeled "loop for radially averaged FPS".
- Lines 22-24: `co(co==0)=1`, `pdr = pdr ./ co;`, and `pdr=pdr(2:end-1);` are grouped by a bracket pointing to a box labeled "1D radially averaged FPS".
- Lines 25-26: `f=2:length(pdr)+1;` and `f=f/length(pdr)/2;` are grouped by a bracket pointing to a box labeled "prepare frequency or wavenumber".
- Line 27: `bpd0=binaverageM(f,pdr,20);` points to a box labeled "bin averaged FPS".
- Lines 29-32: `bpd=bpd0.d(xi);`, `bin=bpd0.bb(xi);`, `f=f*fs;`, and `bin=bin*fs;` are grouped by a bracket pointing to a box labeled "prepare output".

Figure D3. A Matlab code to estimate the 2D Fourier power spectrum and to perform a radially average.

- 656 Arabian Sea and Bay of Bengal and their evolution during SW Monsoon: a novel
657 application of along-track Radar Altimeter measurements from space. *International*
658 *Archives of the Photogrammetry, Remote Sensing & Spatial Information Sciences*,
659 *XL-8*, 1027–1033.
- 660 Bigg, G., Jickells, T., Liss, P., & Osborn, T. (2003). The role of the oceans in climate.
661 *International Journal of Climatology: A Journal of the Royal Meteorological Society*,
662 *23*(10), 1127–1159.
- 663 Bolgiano, R. (1959). Turbulent spectra in a stably stratified atmosphere. *Journal of*
664 *Geoscience Research*, *64*, 2226–29.
- 665 Brown, G. (1977). The average impulse response of a rough surface and its applications.

- 666 *IEEE Transactions on Antennas and Propagation*, 25(1), 67–74.
- 667 Calif, R., & Schmitt, F. G. (2012). Modeling of atmospheric wind speed sequence using a
668 lognormal continuous stochastic equation. *Journal of Wind Engineering and Industrial*
669 *Aerodynamics*, 109, 1–8.
- 670 Carter, D. (1982). Prediction of wave height and period for a constant wind velocity using
671 the JONSWAP results. *Ocean Engineering*, 9(1), 17–33.
- 672 Charney, J. G. (1971). Geostrophic turbulence. *Journal of the Atmospheric Sciences*, 28(6),
673 1087–1095.
- 674 Chelton, D. B., Freilich, M. H., Sienkiewicz, J. M., & Von Ahn, J. M. (2006). On the
675 use of QuikSCAT scatterometer measurements of surface winds for marine weather
676 prediction. *Monthly Weather Review*, 134(8), 2055–2071.
- 677 Danilov, S. D., & Gurarie, D. (2000). Quasi-two-dimensional turbulence. *Physics-Uspekhi*,
678 43(9), 863.
- 679 Davies, L., & Gather, U. (1993). The identification of multiple outliers. *Journal of the*
680 *American Statistical Association*, 88(423), 782–792.
- 681 Egolf, P. W., & Hutter, K. (2020). *Nonlinear, nonlocal and fractional turbulence: Alternative*
682 *recipes for the modeling of turbulence*. Springer Nature.
- 683 Formenti, D. (1999). What is the coherence function and how can it be used to find
684 measurement and test setup problems? *Sound and Vibration*, 33(12), 2-3.
- 685 Freilich, M., & Chelton, D. (1986). Wavenumber spectra of Pacific winds measured by the
686 Seasat scatterometer. *Journal of Physical Oceanography*, 16(4), 741–757.
- 687 Frisch, U. (1995). *Turbulence: the legacy of AN Kolmogorov*. Cambridge University Press.
- 688 Hanley, K. E., Belcher, S. E., & Sullivan, P. P. (2010). A global climatology of wind–wave
689 interaction. *Journal of Physical Oceanography*, 40(6), 1263–1282.
- 690 Hastenrath, S. (1999). Dynamics of the Pacific equatorial dry zone. *Meteorology and*
691 *Atmospheric Physics*, 71(3), 243–254.
- 692 Hauser, D., Tison, C., Amiot, T., Delaye, L., Mouche, A., Guitton, G., ... Castillan,
693 P. (2016). CFOSAT: A new Chinese-French satellite for joint observations of ocean
694 wind vector and directional spectra of ocean waves. In R. J. Frouin, S. C. Shenoi,
695 & K. H. Rao (Eds.), *Remote sensing of the oceans and inland waters: Techniques,*
696 *applications, and challenges* (Vol. 9878, pp. 117–136). SPIE.
- 697 Hauser, D., Tourain, C., Hermozo, L., Alraddawi, D., Aouf, L., Chapron, B., ... Tran,
698 N. (2020). New observations from the SWIM radar on-board CFOSAT: instrument
699 validation and ocean wave measurement assessment. *IEEE Transactions on Geoscience*
700 *and Remote Sensing*.
- 701 Huang, Y., Schmitt, F. G., Hermand, J.-P., Gagne, Y., Lu, Z., & Liu, Y. (2011). Arbitrary-
702 order Hilbert spectral analysis for time series possessing scaling statistics: Comparison
703 study with detrended fluctuation analysis and wavelet leaders. *Physical Review E*,
704 84(1), 016208.
- 705 Huang, Y., Schmitt, F. G., Lu, Z., & Liu, Y. (2008). Scaling analysis of time series using
706 empirical mode decomposition and Hilbert spectral analysis. *Traitement du Signal*,
707 25(6), 481–492.
- 708 Hwang, P. A., Teague, W. J., Jacobs, G. A., & Wang, D. W. (1998). A statistical comparison
709 of wind speed, wave height, and wave period derived from satellite altimeters and
710 ocean buoys in the Gulf of Mexico region. *Journal of Geophysical Research: Oceans*,
711 103(C5), 10451–10468.
- 712 Khandekar, M. L. (2013). *Operational analysis and prediction of ocean wind waves* (Vol. 33).
713 Springer Science & Business Media.
- 714 Kinsman, B. (1965). *Wind waves: their generation and propagation on the ocean surface*.
715 Englewood Cliffs, N.J. Prentice-Hall.
- 716 Kirchner, J. W. (2005). Aliasing in $1/f^\alpha$ noise spectra: Origins, consequences, and remedies.
717 *Physical Review E*, 71(6), 066110.
- 718 Kolmogorov, A. (1941). Energy dissipation in locally isotropic turbulence. *Doklady Akademii*
719 *Nauk SSSR*, 32, 19–21.

- 720 Kraichnan, R. H. (1967). Inertial ranges in two-dimensional turbulence. *Physics of Fluids*,
721 *10*(7), 1417–1423.
- 722 Kunz, G. J., de Leeuw, G., Becker, E., & O’Dowd, C. D. (2002). Lidar observations of
723 atmospheric boundary layer structure and sea spray aerosol plumes generation and
724 transport at Mace Head, Ireland (PARFORCE experiment). *Journal of Geophysical
725 Research: Atmospheres*, *107*(D19), PAR–11.
- 726 Lang, F., Huang, Y., Siems, S., & Manton, M. (2018). Characteristics of the marine atmo-
727 spheric boundary layer over the southern ocean in response to the synoptic forcing.
728 *Journal of Geophysical Research: Atmospheres*, *123*, 7799–7820.
- 729 Li, X., Xu, Y., Liu, B., Lin, W., He, Y., & Liu, J. (2021). Validation and calibration of Nadir
730 SWH products from CFOSAT and HY-2B with satellites and in-situ observations.
731 *Journal of Geophysical Research: Oceans*, *126*, e2020JC016689.
- 732 Lin, W., & Dong, X. (2011). Design and optimization of a Ku-band rotating, range-gated
733 fanbeam scatterometer. *International Journal of Remote Sensing*, *32*(8), 2151–2171.
- 734 Lin, W., Dong, X., Portabella, M., Lang, S., He, Y., Yun, R., ... Liu, J. (2018). A
735 perspective on the performance of the CFOSAT rotating fan-beam scatterometer.
736 *IEEE Transactions on Geoscience and Remote Sensing*, *57*(2), 627–639.
- 737 Liu, J., Lin, W., Dong, X., Lang, S., Yun, R., Zhu, D., ... others (2020). First results
738 from the rotating fan beam scatterometer onboard cfosat. *IEEE Transactions on
739 Geoscience and Remote Sensing*, *58*(12), 8793–8806.
- 740 Lovejoy, S., & Schertzer, D. (2011). Space-time cascades and the scaling of ECMWF reanal-
741 yses: Fluxes and fields. *Journal of Geophysical Research: Atmospheres*, *116*(D14).
- 742 Lovejoy, S., & Schertzer, D. (2013). *The weather and climate: emergent laws and multifractal
743 cascades*. Cambridge University Press.
- 744 Lovejoy, S., Tuck, A., Hovde, S., & Schertzer, D. (2007). Is isotropic turbulence relevant in
745 the atmosphere? *Geophysical Research Letters*, *34*(15).
- 746 Lovejoy, S., Tuck, A., Schertzer, D., & Hovde, S. (2009). Reinterpreting aircraft measure-
747 ments in anisotropic scaling turbulence. *Atmospheric Chemistry & Physics*, *9*(14),
748 5007–5025.
- 749 Monaldo, F. (1988). Expected differences between buoy and radar altimeter estimates
750 of wind speed and significant wave height and their implications on buoy-altimeter
751 comparisons. *Journal of Geophysical Research: Oceans*, *93*(C3), 2285–2302.
- 752 Monaldo, F. (1990). Corrected spectra of wind speed and significant wave height. *Journal
753 of Geophysical Research: Oceans*, *95*(C3), 3399–3402.
- 754 Monin, A., & Yaglom, A. M. (1971). *Statistical fluid mechanics, vols. 1 and 2* (Vol. 1975).
755 MIT Press, Cambridge, MA.
- 756 Nastrom, G., & Gage, K. S. (1985). A climatology of atmospheric wavenumber spectra of
757 wind and temperature observed by commercial aircraft. *Journal of the Atmospheric
758 Sciences*, *42*(9), 950–960.
- 759 Obukhov, A. (1941). Spectral energy distribution in a turbulent flow. *Izvestiya Akademii
760 Nauk SSSR, Seriya Geografii i Geofiziki*, *5*, 453–466.
- 761 Obukhov, A. (1959). On influence of buoyancy forces on the structure of temperature field
762 in a turbulent flow. *Doklady Akademii Nauk SSSR*, *125*, 1246.
- 763 Patoux, J., & Brown, R. A. (2001). Spectral analysis of QuikSCAT surface winds and two-
764 dimensional turbulence. *Journal of Geophysical Research: Atmospheres*, *106*(D20),
765 23995–24005.
- 766 Pearson, R. K. (2002). Outliers in process modeling and identification. *IEEE Transactions
767 on Control Systems Technology*, *10*(1), 55–63.
- 768 Pearson, R. K., Neuvo, Y., Astola, J., & Gabbouj, M. (2015). The class of generalized
769 Hampel filters. In *2015 23rd European Signal Processing Conference (EUSIPCO)* (pp.
770 2501–2505).
- 771 Pearson, R. K., Neuvo, Y., Astola, J., & Gabbouj, M. (2016). Generalized Hampel filters.
772 *EURASIP Journal on Advances in Signal Processing*, *2016*(1), 1–18.
- 773 Phillips, O. (1985a). The equilibrium range in the spectrum of wind-generated waves.
774 *Journal of Fluid Mechanics*, *4*, 426–434.

- 775 Phillips, O. (1985b). Spectral and statistical properties of the equilibrium range in wind-
776 generated gravity waves. *Journal of Fluid Mechanics*, *156*, 505–531.
- 777 Pinardi, N., & Milliff, R. F. (2004). *Comparing the kinetic energy vs. wavenumber in*
778 *surface wind fields from ecwf analyses and the nasa quikscat scatterometer* (Tech.
779 Rep.). Istituto Nazionale di Geofisica e Vulcanologias.
- 780 Pinel, J., & Lovejoy, S. (2014). Atmospheric waves as scaling, turbulent phenomena.
781 *Atmospheric Chemistry and Physics*, *14*(7), 3195–3210.
- 782 Pinel, J., Lovejoy, S., & Schertzer, D. (2014). The horizontal space–time scaling and cascade
783 structure of the atmosphere and satellite radiances. *Atmospheric Research*, *140*, 95–
784 114.
- 785 Pope, S. B. (2001). *Turbulent flows*. IOP Publishing.
- 786 Ribal, A., & Young, I. R. (2019). 33 years of globally calibrated wave height and wind
787 speed data based on altimeter observations. *Scientific Data*, *6*(1), 1–15.
- 788 Richardson, L. R. (1922). *Weather prediction by numerical process*. Cambridge University
789 Press.
- 790 Schertzer, D., & Lovejoy, S. (1985). Generalised scale invariance in turbulent phenomena.
791 *Physico Chemical Hydrodynamics*, *6*, 623–635.
- 792 Schertzer, D., & Lovejoy, S. (1987). Physical modeling and analysis of rain and clouds by
793 anisotropic scaling multiplicative processes. *Journal of Geophysical Research: Atmo-*
794 *spheres*, *92*(D8), 9693–9714.
- 795 Schlosser, E., Haumann, F. A., & Raphael, M. N. (2018). Atmospheric influences on the
796 anomalous 2016 Antarctic sea ice decay. *The Cryosphere*, *12*(3), 1103–1119.
- 797 Schmitt, F. G. (2007). Direct test of a nonlinear constitutive equation for simple turbulent
798 shear flows using DNS data. *Communications in Nonlinear Science and Numerical*
799 *Simulation*, *12*(7), 1251–1264.
- 800 Schmitt, F. G., & Huang, Y. (2016). *Stochastic analysis of scaling time series: from*
801 *turbulence theory to applications*. Cambridge University Press.
- 802 Spencer, M. W., Wu, C., & Long, D. G. (1997). Tradeoffs in the design of a spaceborne
803 scanning pencil beam scatterometer: Application to seawinds. *IEEE Transactions on*
804 *Geoscience and Remote Sensing*, *35*(1), 115–126.
- 805 Sreenivasan, K. R., & Antonia, R. (1997). The phenomenology of small-scale turbulence.
806 *Annual Review of Fluid Mechanics*, *29*(1), 435–472.
- 807 Suquet, R. R., Hermozo, L., Tourain, C., Tison, C., Hauser, D., Schippers, P., . . . Lachiver,
808 J. M. (2019). CAL/VAL phase for the SWIM instrument onboard CFOSAT. In
809 *IGARSS 2019-2019 IEEE International Geoscience and Remote Sensing Symposium*
810 (pp. 8015–8018).
- 811 Tourain, C., Piras, F., Ollivier, A., Hauser, D., Poisson, J.-C., Boy, F., . . . Tison, C. (2021).
812 Benefits of the Adaptive algorithm for retracking altimeter nadir echoes: results from
813 simulations and CFOSAT/SWIM observations. *IEEE Transactions on Geoscience and*
814 *Remote Sensing*, *59*, 1-14.
- 815 Tournadre, J. (1993). Time and space scales of significant wave heights. *Journal of Geo-*
816 *physical Research: Oceans*, *98*(C3), 4727–4738.
- 817 Vallis, G. K. (2017). *Atmospheric and oceanic fluid dynamics*. Cambridge University Press.
- 818 Wikle, C. K., Milliff, R. F., & Large, W. G. (1999). Surface wind variability on spatial
819 scales from 1 to 1000 km observed during TOGA COARE. *Journal of the Atmospheric*
820 *Sciences*, *56*(13), 2222–2231.
- 821 Wyngaard, J. C. (2010). *Turbulence in the atmosphere*. Cambridge University Press.
- 822 Xu, Y., Fu, L.-L., & Tulloch, R. (2011). The global characteristics of the wavenumber
823 spectrum of ocean surface wind. *Journal of Physical Oceanography*, *41*(8), 1576–1582.
- 824 Xu, Y., Liu, J., Xie, L., Sun, C., Liu, J., Li, J., & Xian, D. (2019). China-France Oceanogra-
825 phy Satellite (CFOSAT) simultaneously observes the typhoon-induced wind and wave
826 fields. *Acta Oceanologica Sinica*, *38*(11), 158–161.
- 827 Zhang, K., Dong, X., Zhu, D., & Yun, R. (2021). Estimation and correction of geolocation
828 errors of the CFOSAT scatterometer using coastline backscatter coefficients. *IEEE*

829
830

Journal of Selected Topics in Applied Earth Observations and Remote Sensing, 14,
53-61.